

Modeling Grid Erosion in the NEXT Ion Thruster Using the CEX2D and CEX3D Codes

James Polk (✉ james.e.polk@jpl.nasa.gov)

Jet Propulsion Lab

Vernon Chaplin

Jet Propulsion Lab

John Yim

NASA Glenn Research Center

George Soulas

NASA Glenn Research Center

George Williams

NASA Glenn Research Center

Rohit Shastry

NASA Glenn Research Center

Research Article

Keywords:

Posted Date: April 6th, 2022

DOI: <https://doi.org/10.21203/rs.3.rs-1517801/v1>

License:  This work is licensed under a Creative Commons Attribution 4.0 International License.

[Read Full License](#)

Modeling Grid Erosion in the NEXT Ion Thruster Using the CEX2D and CEX3D Codes

James Polk^{1*}, Vernon Chaplin¹, John Yim², George Soulas², George Williams² and Rohit Shastry²

^{1*}Jet Propulsion Laboratory, California Institute of Technology, 4800 Oak Grove Dr., Pasadena, 91109, California, USA.

²NASA Glenn Research Center, 21000 Brookpark Rd., Cleveland, 44135, Ohio, USA.

*Corresponding author(s). E-mail(s): james.e.polk@jpl.nasa.gov;

Contributing authors: vernon.h.chaplin@jpl.nasa.gov;
john.t.yim@nasa.gov; george.c.soulas@nasa.gov;
george.j.williams@nasa.gov; rohit.shastry@nasa.gov;

Abstract

NASA's Evolutionary Xenon Thruster (NEXT) is a candidate for future deep space missions that offers high efficiency and specific impulse over a large power throttling range. One of the key life-limiting components is the ion accelerator system, which is subject to sputter erosion by low energy discharge plasma ions incident on the upstream screen grid and higher energy charge exchange ions that impact the downstream accelerator grid. The grid erosion codes CEX2D and CEX3D were validated with data from tests of NEXT as well as the NSTAR ion thruster and then used to assess the time to failure due to screen grid erosion and electron backstreaming caused by accelerator grid aperture erosion. Screen grid erosion was found to be important only at the lowest throttle levels, and was conservatively estimated to lead to failure after processing over 900 kg of xenon. The first failure mode at high power levels was

found to be electron backstreaming due to accelerator grid hole wall erosion, which would occur after processing over 700 kg of propellant.

1 Introduction

NASA's Evolutionary Xenon Thruster (NEXT) and the associated power processing unit, propellant management assembly, and prototype gimbal were developed to support ambitious future deep space missions. NASA Glenn Research Center (GRC) and Aerojet Rocketdyne continuing development under the NEXT-Commercial (NEXT-C) program, which is designed to provide hardware for NASA and commercial customers. The NEXT-C ion propulsion system is being demonstrated on the Double Asteroid Redirect Test (DART) mission, which was launched in 2021. [1]

NEXT is a xenon engine with two-grid, outward-dished ion optics and can be throttled from 0.5-6.9 kW input power to accommodate variations in solar array output with solar range. Over this power range it produces thrust values from 25-237 mN and specific impulses from 1300-4150 seconds. Throttling is accomplished by varying beam voltage and current over 40 discrete throttle levels (TLs) [2], as displayed in Fig. 1.

Engine service life is being established by a combination of test and analysis, in accordance with NASA recommendations for life qualification [3, 4]. A key part of this effort was the NEXT Long-Duration Test (LDT), which was initiated in June 2005 to help identify potential failure modes, define failure mode drivers, and validate failure models. The test article was a modified version of an engineering model (designated EM3) which incorporated prototype-model (PM) ion optics and a graphite discharge cathode keeper electrode. More detailed descriptions of the hardware and the vacuum facility can be found elsewhere [5–10]. The thruster was operated over a range of throttle levels representative of candidate mission profiles [11] for the first 29,000 hours and then at full power for a total of 51,184 hours [12]. A total of 918 kg of propellant was processed, demonstrating a total impulse of 35.5 MN-s. The operating conditions are summarized in Table 1. Individual segment lengths were chosen to characterize performance changes and wear rates to provide validation data for life models.

The NEXT LDT was conducted in a vacuum facility at NASA GRC which incorporates a graphite beam target to minimize backspattering. Despite this, carbon backspatter rates of up to 2.8 $\mu\text{m}/\text{kh}$ were measured in the LDT, as shown in Table 1. As a result, carbon deposits up to 70% of the accelerator grid thickness accumulated on the ion optics, making interpretation of the erosion difficult. To help unravel the grid erosion from the carbon deposition and predict erosion rates in space, we employed two ion optics models that

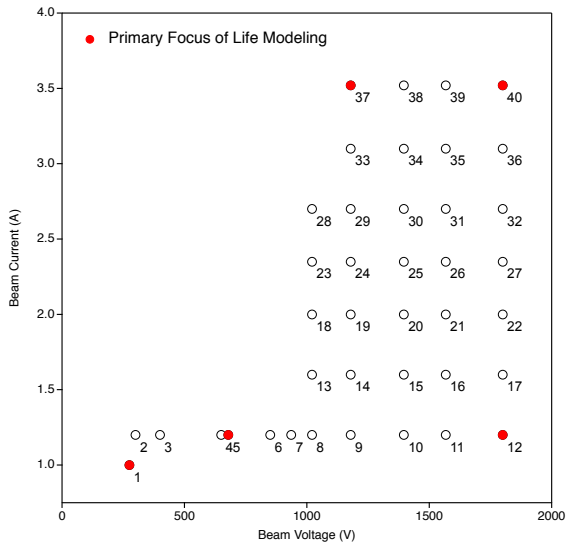


Fig. 1 NEXT throttling envelope in terms of beam voltage and current. 40 discrete throttle levels allow operation over an input power range of 0.5 to 6.9 kW.

Table 1 Operating Conditions for the NEXT Long Duration Test Segments

Throttle Level	Thruster Power (kW)	Beam Current and Voltage	Segment Duration (Hrs)	Cumulative Duration (Hrs)	Segment Throughput (kg)	Cumulative Throughput (kg)	Backsputter Rate ($\mu\text{m}/\text{kh}$)
40	6.9	3.52 A, 1800 V	13,042	13,042	264.7	264.7	2.8
37	4.7	3.52 A, 1179 V	6,478	19,520	132.6	397.3	1.2
5	1.1	1.20 A, 679 V	3,411	22,931	26.7	424.0	0.2
1	0.5	1.00 A, 275 V	3,198	26,129	23.4	447.4	0.1
12	2.4	1.20 A, 1800 V	3,111	29,240	24.5	471.9	1.0
40	6.9	3.52 A, 1800 V	21,944	51,184	446.3	918.2	2.8

have been developed at the Jet Propulsion Laboratory (JPL) over the last 18 years, CEX2D and CEX3D. These are two- and three-dimensional models of individual ion beamlets that simulate the primary ions, the neutral gas flow from the engine and the ambient neutral gas, charge exchange reactions between primary ions and neutrals, and the sputter erosion of the grids caused by impact of the charge exchange ions. The specific objectives of the modeling effort described here were to determine how carbon deposition during the NEXT LDT influenced the wear rates, extract data from the LDT results that could be used to validate the CEX2D and CEX3D codes, use data from other tests to help validate the codes, and model erosion for in-space conditions with the validated codes.

The primary focus of this effort was on modeling the five throttle points shown in red in Fig. 1, which match the five conditions tested in the LDT and represent extremes in currents or voltages that can result in worst case erosion

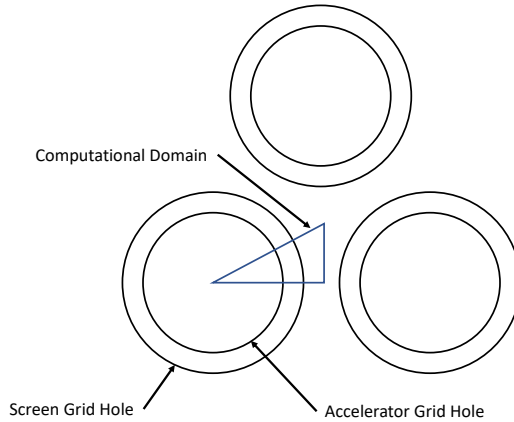


Fig. 2 The computational domain of CEX3D is a triangular prism representing 1/12 of an aperture in the hexagonal pattern.

rates. In this paper we report the results for screen grid erosion and electron backstreaming due to accelerator grid aperture wall erosion, two primary potential failure modes. We also modeled erosion in the pits and grooves pattern that forms on the downstream face of the accelerator grid, as reported in an earlier paper [13]. The results presented here are deterministic predictions of time to failure in space, based on nominal code input parameters. A preliminary probabilistic analysis of electron backstreaming failure that incorporates the variability in some of the input parameters is discussed in another paper [14].

2 The CEX2D and CEX3D Codes

CEX2D [3, 15, 16] models an axisymmetric beamlet and solves Poisson's equation in cylindrical coordinates, while CEX3D [13, 17] uses 3D Cartesian coordinates and simulates a triangular wedge spanning 1/12 of the beamlet (the minimum domain necessary to capture the 3D beamlet properties, taking advantage of the hexagonal symmetry of the grid hole pattern [18]), as shown in Fig. 2. The computational mesh in CEX3D is made up of 30-60-90 triangular prisms with constant transverse dimensions dx and dy . The mesh in CEX2D consists of rectilinear elements with constant radial dimensions dr . Both codes use variable axial mesh spacing dz , with progressively larger mesh volumes in the region downstream of the grids where the ion density is low.

The computational models consist of separate modules that solve for the primary beam ion trajectories, the neutral gas density distribution, and the charge exchange ion trajectories, as outlined in Fig. 3. The beam and neutral gas models provide the inputs needed for the charge exchange ion model, and grid erosion due to both beamlet ions and charge exchange ions is calculated. CEX2D can carry out time-dependent erosion simulations [16] in which the

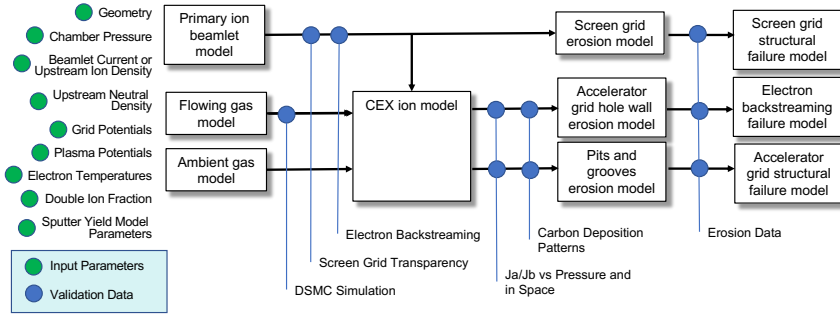


Fig. 3 Schematic of the CEX2D and CEX3D code modules, input parameters, and validation data.

particle trajectories and potential are updated as the grid geometry changes. This approach is not yet computationally feasible for the 3D simulations, so the time-dependent wear is estimated using a separate code that calculates sputtering and redeposition in the pits and grooves pattern from the impinging ion current density calculated by CEX3D at $t = 0$.

2.1 Ion Beamlet Model

Both codes use a “flux tube” approximation [18, 19] for the beam ion solution. Macroparticles are pushed through a static potential with charge density assigned to each mesh node in proportion to the time each macroparticle spends in its vicinity, then the potential solution is updated and the process is repeated until convergence. The beam ion macroparticles enter the domain at the upstream boundary with uniform number density and axially directed Bohm velocity $c_s = \sqrt{kT_e/m_i}$, where k is Boltzmann’s constant, T_e is the electron temperature, and m_i is the ion mass. The more mobile electrons are assumed to follow a Boltzmann density distribution as a function of potential ϕ , $n_e(\phi) = n_{e0} \exp[e(\phi - \phi_0)/kT_e]$, where different electron temperatures, reference densities n_{e0} , and potentials ϕ_0 are used for the regions upstream and downstream of the grids. The electron density is assumed to be zero at locations between the downstream face of the screen grid and the axial location of the potential minimum $\phi_{\min}(x, y)$.

The nonlinear Poisson’s equation that results from the Boltzmann expression is linearized through a Taylor expansion [13] and solved using the PARDISO parallel sparse direct solver, [20, 21] included in the Intel Math Kernel Library (MKL). The potential solver uses constant (Dirichlet) boundary conditions at the upstream and downstream edges of the domain, and zero derivative (Neumann) boundary conditions at the symmetry boundaries. Macroparticles that contact the grids or cross the upstream or downstream boundaries are removed from the simulation, while those incident on other boundaries are specularly reflected, simulating an ion from an adjacent beamlet (or from another part of the same beamlet in the case of CEX3D) entering the domain while the original ion exits.

2.2 Neutral Gas Models

The model [13, 22] for the contribution to the neutral gas density n_{gas} due to flow through the grids assumes that the downstream boundary of the accelerator grid hole acts like a disk-shaped particle sink on the upstream side and as an effusive particle source on the downstream side. The magnitude of the flow through the apertures is assumed to be equal to the thermal flux at the specified upstream neutral density (with a gas temperature based on the discharge chamber wall temperature) scaled by a Clausing factor calculated using a Monte Carlo simulation for an approximate grid geometry. The velocity distribution of the gas flowing from the thruster in CEX3D is assumed to be a drifting Maxwellian, with mean velocity obtained from the Clausing factor calculation. Based on the 3D Monte Carlo simulation results described below, we set the gas temperature in the downstream region to be $2/3$ of the discharge chamber gas temperature.

The contribution to the neutral density due to the ambient gas population flowing toward the grids in ground test facilities is assumed to have a 300 K half-Maxwellian velocity distribution in the axial direction and 300 K full Maxwellian distribution in the other two directions, with density equal to half of the background neutral density in the test chamber. All background gas flowing away from the thruster is assumed to have reflected off the accelerator grid with a half-Maxwellian velocity distribution at the grid temperature in the axial direction and a full Maxwellian distribution at this temperature in the other two directions. The density of the outflowing background population is chosen to make the flux of gas toward and away from the thruster equal (leakage of some incident gas through the grids into the discharge chamber is neglected).

2.3 Charge Exchange Ion Model

In CEX2D and CEX3D, the converged beam ion solution is used along with the neutral gas density model to calculate the charge exchange ion birth rate per unit volume according to:

$$\dot{n}_{\text{CEX}} = n_{\text{beam}}\sigma_{\text{CEX}}(E_{\text{beam}})v_{\text{beam}}n_{\text{gas}}, \quad (1)$$

where n_{beam} is the primary beam ion density, σ_{CEX} is the charge exchange cross section, which depends on the beam ion energy E_{beam} , and v_{beam} is the beam ion velocity. The charge exchange cross sections for the symmetric processes $\text{Xe}^{n+} + \text{Xe} \rightarrow \text{Xe} + \text{Xe}^{n+}$ ($n = 1$ or 2) are calculated using formulas developed by Miller [23] from measured cross sections, and the energy and velocity of beam ions are calculated from the beamlet potential solution using energy conservation [13]. During the charge exchange ion calculation, both the beam ion density and neutral gas density distributions are treated as static. This is justified because only a small fraction of beam ions and neutral gas atoms undergo charge exchange reactions as they transit the simulation domain.

CEX2D pushes charge exchange ion macroparticles through a beamlet potential distribution that is also treated as static. The neglected charge exchange ion space charge has little impact on hole wall erosion, since beam ion contributions to the potential dominate in the non-neutral region very near the accelerator grid. On the other hand, charge exchange ions that cause pits and grooves erosion can be born far downstream (several cm) of the grid, and the perturbations to the potential in this region caused by their space charge, while small ($\ll 10$ V), can have an important effect on both the total flux and spatial distribution of charge exchange ions striking the accelerator grid. Therefore, a full particle-in-cell (PIC) [24] model for the charge exchange ions was recently implemented in CEX3D as described by Chaplin [13].

In the latest version of CEX2D the initial velocity v_0 of each charge exchange ion is assumed to be equal to the mean velocity of the neutral gas flow downstream of the grids. CEX3D incorporates a more detailed model that randomly selects the charge exchange ion velocity component in each direction from a distribution that accounts for both the finite temperature of the gas and the non-zero momentum transfer in charge exchange collisions [25–27]. The code includes velocity rescaling for the slow charge exchange ions to allow larger time steps, as described in detail by Chaplin [13].

2.4 Grid Erosion Model

In both codes, when a beam ion or charge exchange ion macroparticle strikes a grid, it is removed from the computation, and the sputtered grid mass is calculated using the semi-empirical formula developed by Eckstein [28] for sputter yield. CEX2D corrects the grid erosion rates for the presence of doubly-charged ions, taking advantage of the fact that particles of different charge-to-mass ratio starting from rest follow the same trajectories in a steady state electrostatic field [13, 16]. This correction is required to accurately calculate the screen grid erosion rate from incident beam ions, due to the very strong energy dependence of the sputtering yield at low energies [29]. It is much less important at the energies relevant for ions striking the downstream face of the accelerator grid, so it is not accounted for in the accelerator grid erosion calculations in CEX3D.

In order to follow the time evolution of the grid geometry, CEX2D keeps track of the mass on each mesh node, which is reduced each time there is a sputtering event. Nodes within the grid are fixed at the grid potential until their mass reaches zero, at which time they are re-classified as free space nodes and the potential is updated according to Poisson's equation. Because the potential is not updated until a cell is completely removed, sudden jumps of a few volts in the calculated electron backstreaming limits can occur.

The codes account for the angle-of-incidence dependence in the sputter yield using the Wei formula [30]. As the grid shape evolves in time in the 2D code,

the direction of the surface normal at each location is estimated by drawing a vector from the local center of mass to the center of the edge cell of interest [31].

In CEX2D, the mass loss rate of the accelerator grid is reduced by a constant factor to account for the average rate of redeposition of sputtered atoms on the hole walls. The hole wall redeposition fraction is estimated analytically by approximating the accelerator grid hole as a perfect cylinder, assuming sputtering occurs uniformly over the surface, and assuming all sputtered atoms are emitted at an angle 60 degrees offset from the surface normal (approximating the under-cosine distribution peaking at 60 degrees that has been measured for normal-incidence sputtering [32]). Unlike CEX2D, CEX3D currently does not account for redeposition.

2.5 Electron Backstreaming Model

Electron backstreaming occurs when the magnitude of the negative potential inside the accelerator grid holes becomes small enough that a non-negligible current of plume electrons can flow upstream through the grids. Electron backstreaming reduces the thruster's electrical efficiency and can produce unacceptably high heat loads in the discharge chamber, thus ending the useful life of the engine. CEX2D calculates the electron backstreaming current [15] by integrating the electron flux over a surface defining the minimum potential $\phi_{\min}(r)$ inside the accelerator grid hole as a function of radius.

Assuming a thermal electron population downstream of the grids, with temperature $T_{e,\text{down}}$ everywhere and density $n_{e,\text{down}}$ and potential far downstream from the grids ϕ_{down} , the backstreaming current through an axisymmetric differential area dA on the minimum potential surface is

$$dI_{\text{EBS}} = \frac{dA}{4} \sqrt{\frac{8kT_{e,\text{down}}}{\pi m_e}} \times \left(en_{e,\text{down}} \exp\left(-\frac{e(\phi_{\text{down}} - \phi_{\min}(r))}{kT_e}\right) \right). \quad (2)$$

The code integrates this expression over the minimum potential surface using $dA = 2\pi r dl = 2\pi r \sqrt{dr^2 + \Delta z^2}$, where dr is the radial mesh spacing and Δz is the axial spacing between minimum potential points at adjacent radial locations. When carrying out the discretized calculation for the electron flux through each area element, $\phi_{\min}(r)$ is evaluated as the average of the potentials at the two nodes bounding the element.

In order to calculate the electron backstreaming limit V_{EBS} , CEX2D reduces the magnitude of the accelerator grid voltage in one volt steps until electron backstreaming occurs. In this work, V_{EBS} for a single beamlet is defined to be the accelerator grid voltage V_a at which the electron backstreaming current is 1% of the beamlet current. Changing this threshold to 0.1% or 10% would only

change the calculated electron backstreaming limit by a few volts because of the exponential dependence of the electron backstreaming current on potential in Eq. 2. This exponential growth of electron backstreaming current with V_a also implies that once the electron backstreaming current threshold has been exceeded for beamlets at some radial location on the grid, the accelerator grid voltage will need to be increased only slightly for the electron backstreaming threshold for the entire beam to be exceeded. Therefore, for these simulations we make the approximation that the most negative electron backstreaming limit calculated for any single beamlet on the grid is equal to the overall electron backstreaming limit for the thruster. The code's electron backstreaming limit calculation also accounts for the effect of thinning of the screen grid, which tends to increase electron backstreaming at a given accelerator grid voltage by allowing the influence of the high upstream discharge potential to penetrate further into the accelerator grid hole. Reducing the grid gap has a similar effect.

2.6 Code Verification

The simulation input parameters and the new algorithms incorporated in the codes for this work were tested to verify that the physics models described above were properly implemented. New simulation results obtained with the PARDISO sparse matrix solver [21] were found to be identical to older simulations that used a slower solver from the Compaq Extended Math Library (CXML). A revised calculation correcting for the effect of grid curvature on the axial potential gradient in the beam was verified by showing that the results obtained with beam ions alone matched the analytical result of a Boltzmann relation dependence on ion density [13]. The algorithm in CEX3D for rescaling charge exchange ion velocities in order to improve the PIC calculation simulation time was verified by comparing results obtained with different rescaling thresholds. Even with an aggressive threshold of 1 km/s, only minor differences were observed in the current density pattern on the downstream face of the accelerator grid [13].

Parametric studies revealed the mesh resolution required to obtain smooth potential contours without spurious spatial oscillations. We found that cell dimensions of about half a Debye length in the upstream region were sufficiently small. Further reductions in the mesh spacing did not significantly change the simulation results. Similar studies verified that the choices for the following parameters were not affecting the results:

- Beam ion and charge exchange ion macroparticle size (i.e., the number of macroparticles in the calculations)
- Particle pushing time step
- Simulation domain length
- CEX3D PIC simulation runtime (verifying that the potential solution and the accelerator grid current reached a steady state)

3 Model Validation

Types of data used to validate individual model components and the system-level output are shown in Fig. 3. We compared predicted screen grid and accelerator grid hole wall erosion rates with experimental measurements to validate the primary code outputs, but we also used measurements of intermediate quantities which validate individual code modules. These included measurements of electron backstreaming voltage and screen grid transparency, which test the primary ion beamlet model, and carbon deposition patterns from ground testing, which can also be compared with model predictions. Some code components, such as the neutral gas model, are difficult to validate because there are no detailed measurements. In this case we used a higher fidelity direct simulation Monte Carlo (DSMC) code to validate the more approximate model used in the CEX2D and CEX3D codes.

The validation data were from four tests of two different thrusters—the 8200 hour test of an engineering model NSTAR thruster (the NSTAR LDT), the 30,352 hour Extended Life Test (ELT) of the Deep Space 1 flight spare NSTAR engine, a 2000 hour test of a laboratory model (LM) NEXT thruster, and the 51,184 hour NEXT LDT. The validation data sets consisted of beginning-of-life (BOL) screen grid transparency and electron backstreaming voltage measurements over a range of throttle levels, variations in electron backstreaming voltage during the wear tests, and post-test measurements of screen grid and accelerator grid aperture erosion patterns.

The validity of the input parameters is as important as the predictive capability of the models, particularly for the primary drivers of the erosion processes. Therefore, the validation activity also included a critical assessment of the input parameters' pedigree for the validation cases. Key input parameters are shown on the left in Fig. 3.

3.1 Input Parameters for the Validation Cases

The codes require input parameters which define the optics geometry, the potentials applied to the thruster components, plasma properties in the discharge chamber and the beam, and the neutral gas properties. The sources of data used to define these parameters for each of the tests used in the model validation are summarized in Appendix A.

The codes approximate the cusped geometry of the grids as shown in Fig. 4. In the NSTAR LDT the screen grid suffered very little erosion in the webbing center and the area around each aperture of the accelerator grid experienced net deposition of carbon backsputtered from the facility, so grid thicknesses were based on post-test measurements of the cross-sectioned grids in a scanning electron microscope (SEM) [33]. The screen grid apertures also remained largely intact, so the aperture geometry was based on the post-test measurements. The accelerator grid apertures eroded significantly and diameters were not measured before the test, so the BOL minimum diameter at the cusp

was assumed to be equal to the specification. The upstream and downstream diameters were estimated from post-test measurements [33]. The NSTAR ELT aperture dimensions were based on pre-test measurements of the minimum diameter using precision pins and post-test SEM measurements of the cross-sectioned grids [34]. There were no measurements of grid thickness from the NEXT 2000 hour test, so the values in the manufacturing specification were used. The aperture geometries were based on pre-test precision pin measurements and post-test photos. For the NEXT LDT simulations we used pre-test screen grid thickness measurements from the grid periphery and corrected the thickness in the center for slight thinning due to the grid dishing process. The accelerator grid thickness was based on post-test SEM measurements. The aperture geometries were based on a combination of pin measurements for the minimum diameters, measurements of accelerator grid aperture shapes using putty castings, and post-test measurements of screen grid hole shapes.

The grid gap when the grid assembly is hot is a key geometric parameter, particularly for electron backstreaming calculations, and is one of the most difficult to measure. For the NSTAR cases we performed a parametric study the effect of grid gap on BOL electron backstreaming voltage for the NSTAR LDT. The value that produced the best agreement at BOL also reproduced the measured changes in backstreaming voltage over the course of the test, as shown below in section 3.4. This value is somewhat larger than that measured in an NSTAR LM thruster at full power by monitoring the motion of a ceramic pin that was attached to the center screen grid aperture and protruded through the accelerator grid aperture [35]. The grid gap inferred from the NSTAR LDT BOL backstreaming voltage was also used in the ELT simulations and yielded good agreement with data. In these simulations the hot grid gap was assumed to be constant in time, although post-test measurements of the cold gap showed it had decreased by about 30% at some point in the test, potentially due to residual stresses in the optics assembly [34]. The hot grid gap in the NEXT simulations was based on optical measurements during the LDT [36]. The radius of curvature of the dished grids and the beam diameter in all simulations were based on the manufacturing specification.

The beam and accelerator grid voltages in the simulations were set equal to the throttle table values, which were used as controlled parameters in the wear tests. The discharge voltage was based on either average values for a given test or test segment (NSTAR) or the BOL values (NEXT tests). The beamlet current is a model input for CEX2D, which iterates the upstream plasma density until it produces that beamlet current. The values in all cases were based on Faraday probe measurements in the plume near the grids. The measured beam current densities were extrapolated back to the grid surface and converted to individual beamlet currents [12, 15, 37–39]. CEX3D requires the upstream plasma density as an input. In the simulations for these cases the plasma density corresponding to a given beamlet current in CEX2D was used and the output of CEX3D was checked to verify that it produced the desired beamlet

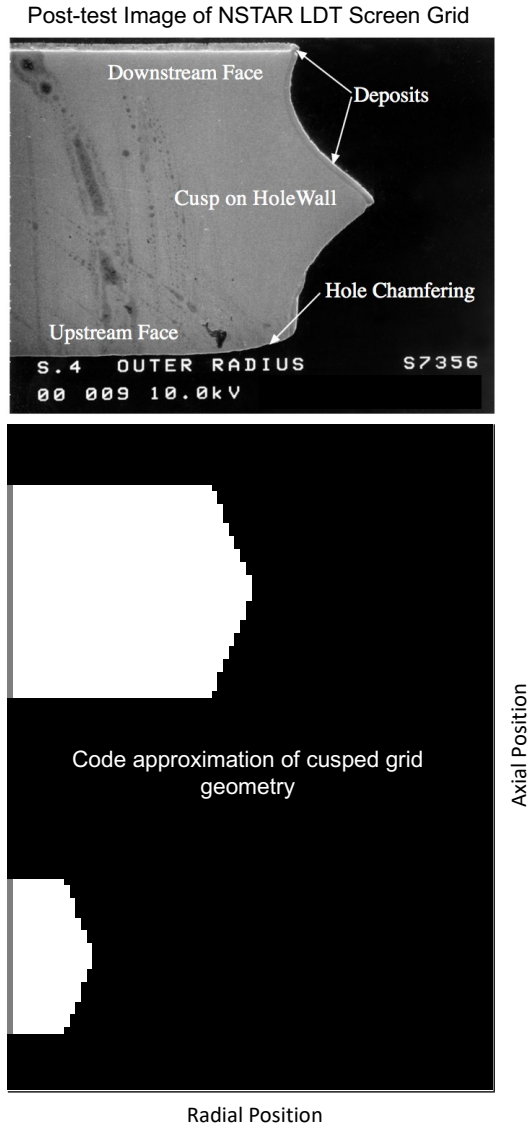


Fig. 4 Cross section of screen grid showing cusped geometry and idealized code geometry.

current. The upstream plasma potential was assumed to be equal to the sum of the beam voltage and the discharge potential. Emissive probe measurements in NSTAR and NEXT thrusters showed that the plasma potential near the grids was within ± 1 V of the discharge voltage [40, 41]. The upstream electron temperature was assumed to be 5 eV for all simulations. Langmuir probe measurements in an NSTAR LM thruster yielded temperatures of 3 - 5 eV [40] and 4 - 6 eV in a NEXT LM thruster [41]. Sensitivity tests showed that the code results were not particularly sensitive to the upstream temperature. The screen grid erosion is strongly influenced by the double ion content of the plasma,

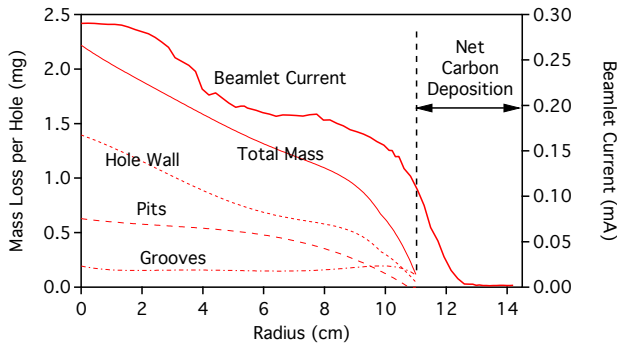


Fig. 5 NSTAR LDT accelerator grid mass loss distribution compared to the current density distribution.

however. In all cases the double-to-single ion current ratio was based on ExB probe measurements conducted on LM or EM thrusters [15, 33, 42].

The downstream plasma potential input is used to specify the downstream boundary condition and was based on emissive probe measurements in the near-field plume [33, 37, 43]. These measurements generally yielded values of 3 - 5 V relative to the facility ground. All other potentials are referenced to neutralizer cathode common, however, so the coupling voltage V_g (the difference between facility ground and cathode common, which is typically about 10 V) must be added to the measured values. For the NSTAR cases we used a downstream electron temperature of 1.8 eV based on measurements from the plasma diagnostics package on the Deep Space 1 mission [44]. For the NEXT cases we used 2 eV, assuming that it would be similar to the NSTAR electron temperature.

The average neutral density \bar{n}_0 in the discharge chamber can be calculated by equating the free molecular flow through the grids to the neutral flow calculated from the beam current J_b and discharge propellant utilization efficiency η_{ud} . This yields

$$\bar{n}_0 = \frac{4J_b}{\bar{v}_{th}A_g\phi_aKe} \frac{(1 - \eta_{ud})}{\eta_{ud}}, \quad (3)$$

where $\bar{v}_{th} = \sqrt{8kT/\pi m}$ is the thermal velocity, k is Boltzmann's constant, T is the gas temperature, m is the xenon atom mass, A_g is the active grid area, ϕ_a is the accelerator grid transparency to neutrals, $K \approx 0.5$ is the Clausing factor for flow through the grids, and e is the electron charge. The average neutral density was used for all simulations. This is a reasonable approximation for the NEXT thruster, which has a relatively flat beam profile. In the NSTAR thruster, however, the magnetic field design results in a high density of primary electrons on the thruster centerline which could deplete the neutral gas along the axis by ionization. The actual distribution of neutral density across the grid face is not well known. Spectroscopic measurements of neutral density in an NSTAR LM thruster suggest that the density on centerline is on the order

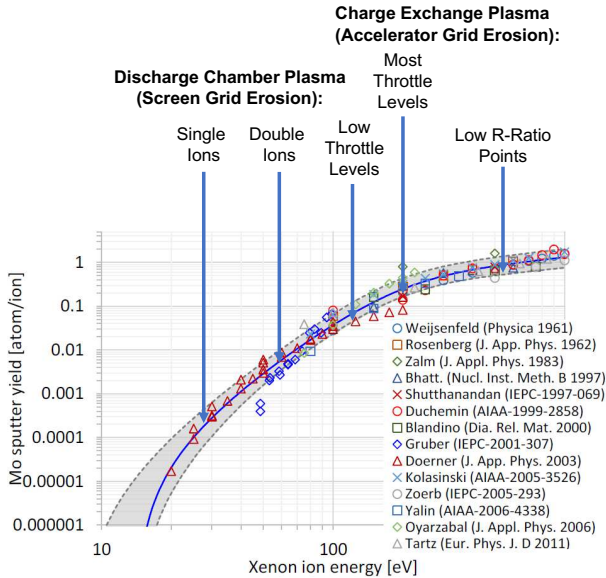


Fig. 6 Maximum likelihood curve fits to sputter yield data for xenon on molybdenum, reproduced from Yim. [29]

of 2.25 times lower than the average density near the grids [45]. A numerical model of the discharge chamber predicted a centerline density over an order of magnitude lower than the average density [46], but such low values are not realistic. Erosion data do not make the picture any clearer. Accelerator grid hole wall erosion should scale with beamlet current and neutral density. However, estimates of the mass loss per hole from the NSTAR LDT accelerator grid based on detailed measurements of the erosion pattern [33] do not show a suppression of erosion compared to the beamlet current on the centerline that would be expected if the neutral density was lower than average there (Fig. 5). As shown in section 3.4, the assumption of a uniform upstream neutral density produces good agreement with data, but this parameter should be considered relatively uncertain compared to other input parameters.

The other contributor to neutral gas densities, the residual xenon gas in the vacuum test facility, is based on measured pressure. In these tests the chamber pressure was measured close to the thruster, so it is representative of the local environment. The NSTAR gauges were calibrated on xenon, while the NEXT gauges were calibrated with nitrogen and the reading corrected for xenon. The neutral gas populations treated in the codes are assumed to have velocities determined by thermal accommodation with the discharge chamber, the accelerator grid, or the vacuum chamber wall. The vacuum chamber was assumed to be room temperature, and the component temperatures were based on NSTAR and NEXT thermal characterization tests [47, 48].

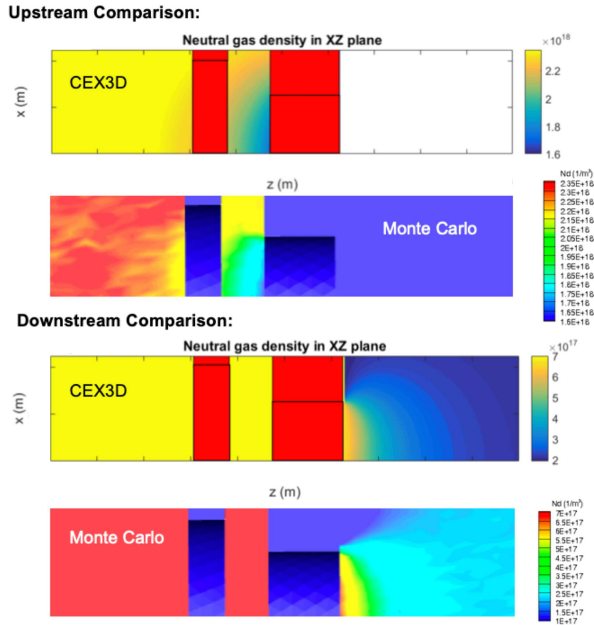


Fig. 7 Comparison of CEX3D neutral model results and more accurate DSMC computation.

One of the most important code inputs is the set of parameters used to model the sputter yield dependence on ion energy and incidence angle. The parameters in the Eckstein and Wei models are based on the curve fits to data for xenon ions on molybdenum by Yim [29]. The data for sputter yield at normal incidence as a function of energy from Yim's review are shown in Fig. 6. The single and double ions that impact the screen grid have energies on the order of 25 and 50 eV, respectively. As shown in Fig. 6, there are very little data in this region and the uncertainties are very large. For the screen grid erosion calculations we used the maximum likelihood curve fit (the solid line). The charge exchange ions striking the accelerator grid are accelerated through the potential difference between where they were created and the accelerator grid, so they have minimum energies on the order of one hundred to several hundred eV, as shown in Fig. 6. There are more data in this range, but the values are scattered. We used the experimental erosion data to help constrain the sputter yield in this energy range, and found that the lower 50% likelihood curve (the lower dashed boundary) produced the best agreement with data for the NSTAR and NEXT tests. The maximum likelihood values for the parameters in the Wei angular dependence model were used for all simulations.

3.2 Neutral Gas Model Validation

It is extremely difficult to directly measure the neutral gas flow through the grids, so there are no detailed data that can be used to validate the neutral

flow model. Instead, we used the high fidelity Direct Simulation Monte Carlo (DSMC) Analysis Code (DAC) to compare with our simpler algorithm. The DAC code implements the DSMC method developed by Bird [49] in a form that can be applied to three dimensional problems. This state-of-the-art tool was developed by NASA and is used to simulate a broad range of rarified gas dynamics problems. It has been extensively validated against other DSMC codes as well as data [50]. We modeled the neutral flow through four holes in a fully 3D simulation with DAC using the NEXT beginning of life aperture geometry as a test case. The upstream parameters matched those used in CEX3D and the grid temperatures were based on NEXT thermal test data [48]. The results of the DAC simulation are compared with the CEX3D results in Fig. 7. The contour levels in the two images at the top are set to the same range and show the same qualitative behavior. The two bottom images compare the much lower density downstream domains. These also agree well qualitatively, with quantitative differences in the regions of interest on the order of 10%.

3.3 Screen Grid Erosion Model Validation

Screen grid erosion is driven primarily by the ion flux to the grid, the double ion content of the plasma, the plasma potential relative to the screen grid, and sputter yields near threshold. The ion flux is sensitive to the screen and accelerator grid geometry, grid gap, the grid voltages, and beam current density. The erosion is weakly dependent on the upstream electron temperature and the calculation does not use the neutral gas model. The screen grid erosion model was validated using screen grid transparency measurements and erosion data from the NSTAR and NEXT wear tests. The grid transparency comparisons test the validity of the upstream plasma and primary beam ion models, while the erosion comparisons test the distribution of ion fluxes on the webbing and the sputtering model.

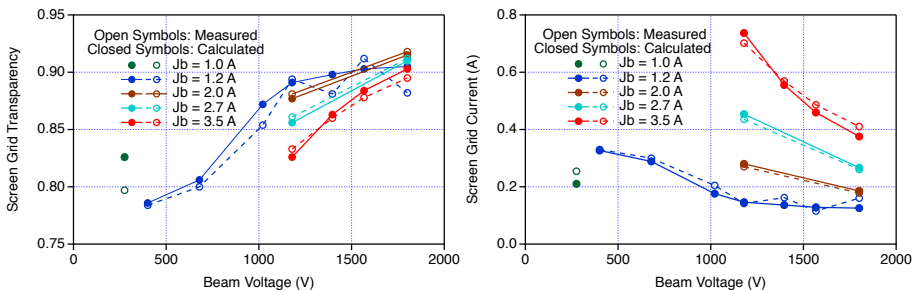


Fig. 8 Measured and calculated screen grid transparency (left) and corresponding screen grid currents (right) for points spanning the NEXT throttle table. The uncertainties in the current and transparency measurements are $\pm 1\%$ and $\pm 1.5\%$, respectively.

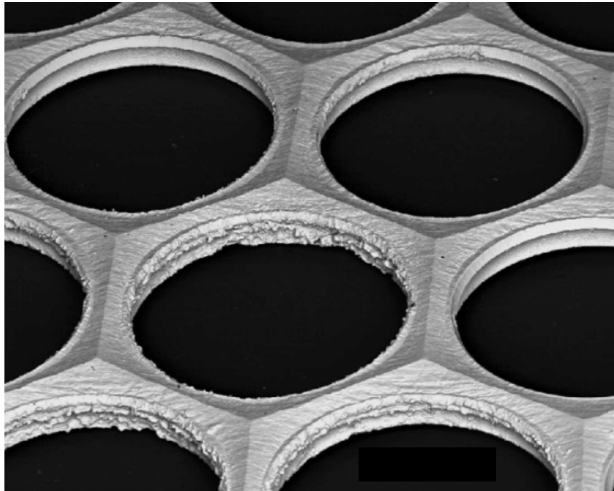


Fig. 9 Upstream surface of the screen grid from the NSTAR LDT showing the typical erosion pattern.

The screen grid transparency ϕ_s is the fraction of total ion current incident on the grid plane that is extracted into the beam,

$$\phi_s = \frac{J_b}{J_b + J_s}, \quad (4)$$

where J_b is the beam current and J_s is the screen grid current, measured by biasing the screen grid negative with respect to the discharge chamber plasma to repel electrons. The CEX2D code was used to calculate the grid transparency for a range of beamlet currents for several NEXT throttle levels and these values were integrated over the grid to determine the average grid transparency. These simulations showed that the transparency calculated for the peak beamlet current was within 1% of the average transparency, so simulations for the peak beamlet current over a much broader range of throttle levels were run. The results are plotted in Fig. 8. The lefthand plot compares the calculated transparencies to the values measured at the beginning of the NEXT LDT. The righthand plot displays the measured screen grid currents and the simulated values scaled with the total beam current. The code reproduces the measured screen grid currents to within about $\pm 5\%$ over a large range of beam currents and voltages.

Erosion on the upstream surface of the screen grid is typically highest at the hole edge and lowest in the center of the webbing, leaving a ridge between apertures. Figure 9 is a scanning electron microscope (SEM) image of a section of the screen grid from the NSTAR LDT showing the characteristic erosion pattern.

The ridge height varies between the thinnest part of the webbing and the region between any three holes, and over certain parts of the grid the edge thickness is slightly different from one side of the aperture to the other in the radial direction, due to deviations from axisymmetry in the beamlet current distribution. We use the CEX2D code to model time-dependent screen grid erosion, so it will not capture the three dimensional variations in grid thickness. However, it should produce a reasonable estimate of the average erosion profile. Figure 10 shows measured edge and ridge erosion as a function of grid radius compared to that calculated using CEX2D. The data marked “ID” represent measurements made on the side of the aperture closest to the grid center, while those labelled “OD” are on the opposite side of the aperture. The plot on the left is from the NSTAR LDT and that on the right is from the NEXT LDT. For the NSTAR case, the code results agree well with measured edge erosion at large grid radii, but overpredict the measured erosion by about 50% in the center. The ridge erosion rate is overpredicted by a factor of 2 - 3 over the entire grid. The errors in calculated screen grid currents are small, so these discrepancies indicate small model errors in the ion current distribution around the hole (resulting in slightly more uniform erosion) and suggest that the actual sputter yield is lower than the value used in the model. This would not be surprising, given the large uncertainties in yield near threshold. The NEXT case shows a similar overprediction of erosion rates by a factor of 2 - 3 over most of the grid, with worse agreement at the grid edges. These results suggest that the double ion fraction may have been lower at the beam edges in this test than the measurements from the EM thruster [42]. In general, however, these comparisons show that the screen grid erosion rates predicted by CEX2D are conservative.

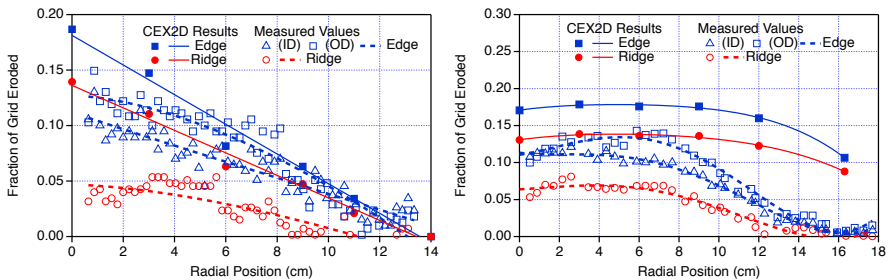


Fig. 10 Comparison of calculated screen grid erosion and post-test measurements from the NSTAR LDT (left) and the NEXT LDT (right). The uncertainty in the measurements is $\pm 3\%$.

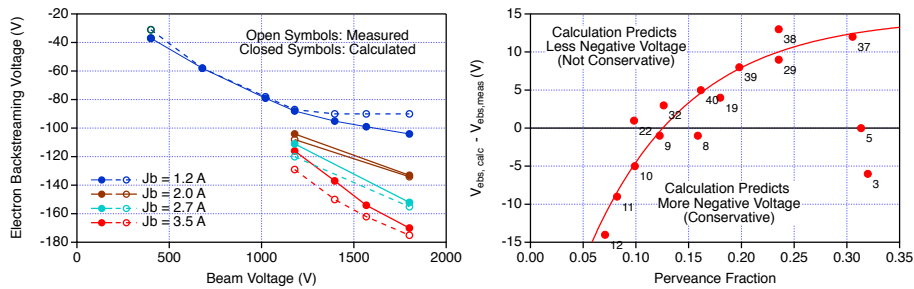


Fig. 11 Comparison of calculated electron backstreaming voltages and measurements from the beginning of the NEXT LDT (left). Difference in measured and calculated backstreaming voltage as a function of perveance fraction. Numbers next to the points are the throttle levels (right). The uncertainty in the electron backstreaming voltage measurements is ± 2.5 V.

3.4 Accelerator Grid Erosion and Electron Backstreaming Model Validation

Accelerator grid hole enlargement is driven by the charge exchange ion flux to the hole wall, the ion energies, and the sputter yields in the 100 - 500 eV range. The ion fluxes depend on the charge exchange rates near the grid (which in turn depend on the beamlet current distribution, aperture geometries, neutral density, and charge exchange cross sections) and the charge exchange ion trajectories. The energies are determined by the potential where the ions are born relative to the accelerator grid potential. The resulting loss of backstreaming margin depends on the evolving geometry and the electric field between the grids (i.e., grid gap and grid potentials). The screen grid transparency comparisons described above test the validity of the primary ion beamlet model and show very good agreement. In this section, we compared measurements of electron backstreaming voltage with CEX2D predictions, which tests the beamlet model, potential solver, and electron backstreaming algorithm. In addition, we compare the code results with measurements of hole erosion and how the electron backstreaming voltage changes with time as a result, which validates the charge exchange ion generation, trajectory tracking, and sputtering models.

Backstreaming electrons produce an additional current in the beam power supply which is indistinguishable from the ion beam current. The backstreaming limit is measured by reducing the magnitude of the accelerator grid voltage in small steps until a slight rise in beam current is observed (typically 0.1 mA [51]) or, for systems with beam current control, a drop in discharge loss occurs (typically 1% [38]). The electron backstreaming voltages measured over a large range of throttle levels at the beginning of the NEXT LDT are plotted on the left side of Fig. 11 with the corresponding CEX2D predictions. The code results agree with the measurements to within ± 15 V over the entire range. The plot on the right in Fig. 11 shows that, with the exception of two lowest voltage throttle points, the difference between the measurements and

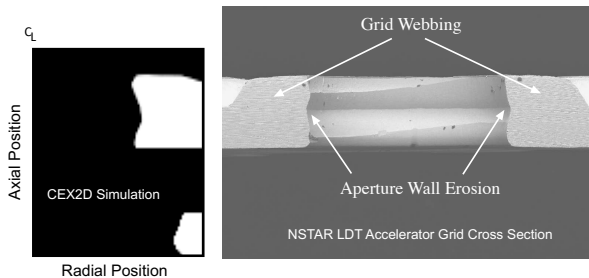


Fig. 12 Accelerator grid geometry after 8200 hours of operation predicted by CEX2D (left) and the actual erosion geometry at the center aperture revealed by cross sectioning the grid from the NSTAR LDT.

calculations is correlated with the perveance fraction,

$$P = \frac{J_{\text{beamlet}}}{J_{\text{beamlet,max}}} = \frac{J_{\text{beamlet}}}{A_s \phi_s j_{\text{max}}}, \quad (5)$$

where J_{beamlet} is the beamlet current, $J_{\text{beamlet,max}} = A_s \phi_s j_{\text{max}}$ is the beamlet current at the perveance limit, based on the screen grid area associated with a single aperture A_s , transparency ϕ_s , and space charge-limited current density $j_{\text{max}} = 4.75 \times 10^{-9} (V_b - V_a)^{3/2} / l_e^2$. The space charge-limited current depends on the beam voltage V_b , the accelerator grid voltage V_a , and the effective grid gap $l_e = [(l_g + t_s)^2 + d_s^2/4]^{1/2}$, where l_g is the actual grid gap, t_s is the screen grid thickness, and d_s is the screen grid aperture diameter. This correlation suggests that the discrepancy is due to small modeling errors in the structure of the primary ion beamlet, which lead to predictions of less negative voltage required to prevent backstreaming at the highest perveance fraction conditions and more negative voltage at the lower perveance fraction points. The code predictions are therefore not conservative for high perveance fractions, so additional margin should be applied. In principle, this correlation could be used to correct the code outputs, yielding agreement to within about ± 5 V, but this was not done in this study.

The time-dependent erosion simulation qualitatively reproduces the erosion profile measured in the NSTAR LDT, as shown in Fig. 12. The left image shows the outline of the grid cross section from CEX2D, while the photo on the right displays an actual cross section of the center hole from the test. The code accurately predicts that the erosion peaks in the middle of the aperture wall and that the hole edges are slightly chamfered. The hole wall erosion was simulated for five radial locations on the grid assuming the average upstream neutral density and sputter yields corresponding to the lower 50% likelihood boundary. The final aperture diameter is compared to post-test precision pin and SEM measurements in the left plot in Fig 13. The agreement is excellent in this case, and we found that these assumptions also reproduced measurements from the NSTAR ELT, the NEXT 2000 hour test, and the NEXT LDT.

The electron backstreaming voltage measured during the NSTAR LDT is shown as a function of time in the right plot in Fig. 13. As the accelerator grid hole diameter increases due to erosion, more negative voltage is required to prevent electrons from backstreaming through the center of the holes. The hot grid gap was not known for this test, but a series of simulations run with the initial grid geometry and varying grid gaps showed that a hot gap of 0.45 mm matched the backstreaming limit measured at the beginning of the test. This gap was then held fixed in time-dependent erosion simulations that produced the erosion data in Fig. 12 and the left plot in Fig. 13. The calculated backstreaming voltages as a function of time displayed in the right plot agree with the measurements to within ± 5 V.

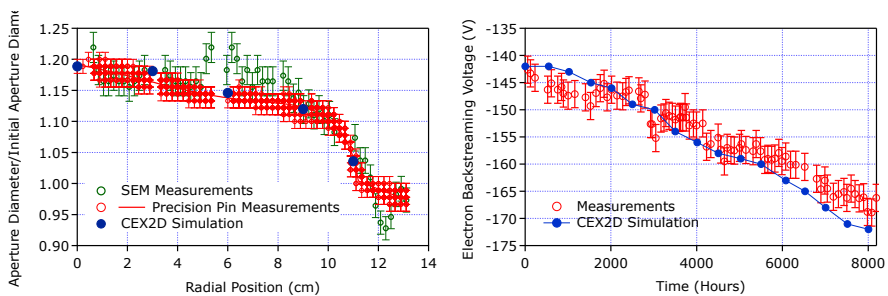


Fig. 13 Comparison of measured and calculated values of the post-test aperture diameter (left) and backstreaming voltage as a function of time (right) for the NSTAR LDT.

The minimum center aperture diameter was measured from photographs taken during the NSTAR ELT and with precision pins after the test [34]. These data are compared with simulations on the left in Fig. 14. The hole diameters calculated with CEX2D are about 5% lower than measured values. We assumed the same initial hot grid gap of 0.45 mm, which matched the backstreaming voltage well in segment 1, as shown on the right. However, we found that 0.4 mm matched segments 2, 3, and 4 better (there are no backstreaming data for segment 5 because it was run at the lowest power and the perveance limit was reached before backstreaming occurred). This change in hot gap is consistent with post-test measurements, which showed a change in the cold grid gap due to residual stresses in grids [34]. The backstreaming voltages calculated with the 0.4 mm grid gap agree well with measurements at the beginning of segment 6, but they diverge toward the end of that segment. This suggests that further changes in the hot grid gap occurred, although the predictions are still within about 10 - 15 V of the measurements. These comparisons show that CEX2D is capable of reproducing accelerator grid hole erosion quite accurately and predicts the electron backstreaming voltage for a given geometry to within about ± 15 V over a wide range of operating conditions.

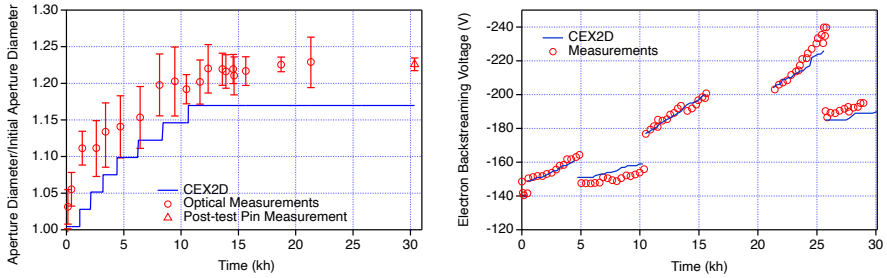


Fig. 14 Comparisons of calculated and measured center aperture erosion (left) and electron backstreaming voltage (right) for the NSTAR ELT. The uncertainty in the electron backstreaming voltage measurements is ± 2.5 V.

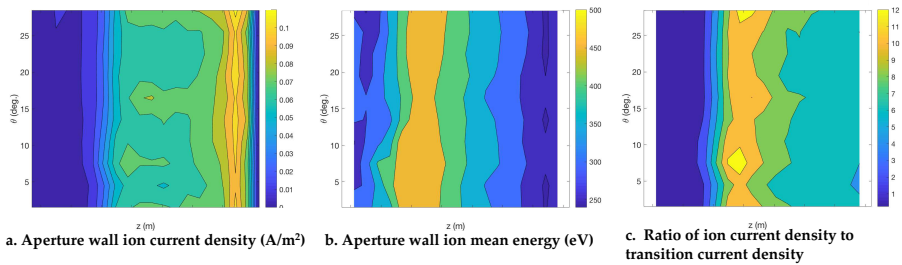


Fig. 15 Impingement current density, mean ion energy, and ratio of current density to the transition current density as a function of position on the hole wall at TL37.

3.5 The Effect of Backspattered Carbon on Accelerator Grid Erosion in the NEXT LDT

Carbon deposits on the accelerator grid in the NEXT LDT cloud the interpretation of hole erosion data. One motivation for this study was to determine whether the simulations can shed light on the impact of the deposits on hole wall erosion. The approach we followed was to use the codes to determine whether the conditions in each test segment would lead to net erosion or net carbon deposition. These predictions were compared with images of the center aperture from each segment to validate the model. The segments that experienced net erosion were then modeled to predict the hole wall erosion, which was compared with optical measurements during the test. CEX3D was used to model the flux, energy, and incidence angle of charge exchange ions that strike the aperture wall in order to capture any three dimensional effects. An example of the code outputs for throttle level TL37 using the beginning of test grid geometry is shown in Fig. 15. The plot in Fig. 15a displays the impingement current density as a function of axial position and azimuthal angle over the 30 degree segment modeled by CEX3D. As Fig. 2 shows, the edges of this segment are symmetry boundaries, so this pattern is repeated around the aperture. In this case the current density peaks near the downstream end of the aperture and is relatively uniform azimuthally. Figure 15b shows the mean ion energy,

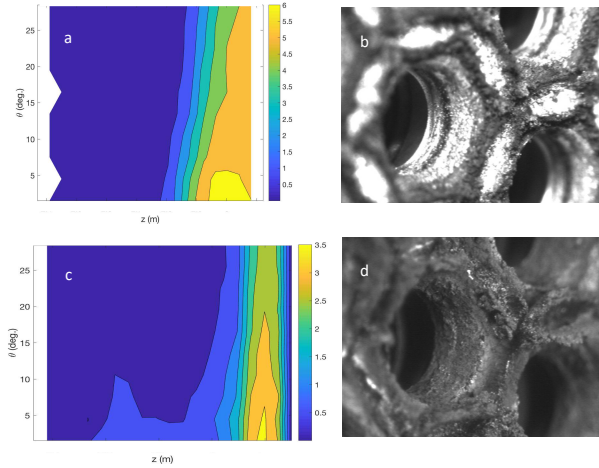


Fig. 16 (a) Predicted ratio of current density to transition current density for the NEXT LDT beginning-of-life geometry at TL40. (b) image of the center hole midway through the first segment. (c) Predicted current density ratio for TL40 with end-of-test geometry. (d) image of the center hole at the end of the test.

which peaks further upstream at about 500 eV. Ions that impact this area are formed in the interelectrode gap where the local potential is about 300 V and are then accelerated into the grid, which is at -210 V.

To determine whether these fluxes and energies are sufficient to prevent net deposition of carbon, we used a model of the surface kinetics of carbon film growth on molybdenum [52]. In steady state, a dynamic equilibrium between the rate of carbon deposition and removal by sputtering will determine the surface coverage of carbon. For sufficiently high fluxes of energetic xenon ions compared to the carbon backsputter rate, the equilibrium surface coverage will be negligible. For ion current densities below a certain threshold at a given energy, however, multiple layers of carbon will start to form and it becomes much more difficult to remove them by sputtering. Under these conditions net deposition will occur and the underlying substrate will be protected from erosion. The threshold current density at which the transition from net erosion to net deposition occurs is given by

$$j_{a,\text{trans}} = \frac{e\gamma_C S_C}{Y_C(E, \theta)} \quad (6)$$

where e is the electron charge, γ_C is the backsputtered carbon flux, S_C is the sticking coefficient for carbon on carbon (taken to be equal to unity) and Y_C is the sputter yield, dependent on energy E and angle θ , for carbon from bulk carbon [52]. To determine the transition current density we used backsputter rates measured during the NEXT LDT with a quartz crystal microbalance and the mean sputter yield based on the maximum likelihood fits to data from

Yim [29] for the simulated ion energies and incidence angles. The ratio of ion current density to the transition current density for TL37 at beginning of life is plotted in Fig. 15c. Values above one indicate that the current density and energy are high enough to prevent net deposition. In this case, most of the aperture wall will experience net erosion; only the upstream end has current densities near the transition value. Because this calculation does not depend on the sputter yield of xenon incident on molybdenum (as comparisons of predicted and measured erosion do), it provides an additional check of the charge exchange ion generation and trajectory models.

Calculations like these were made for the throttle levels tested in the NEXT LDT using the beginning of life grid geometry and an approximation of the end of life geometry, which incorporated larger aperture diameters and a thicker accelerator grid with dimensions based on the average of post-test measurements of the carbon deposits. An example of the analysis is shown in Fig. 16, which compares calculated current ratios and photos of the center aperture from the middle of the first segment at TL40 and the end of the test, after the last segment at TL40. At the beginning of the test the current density distribution and energies are sufficient to prevent net deposition over at least the downstream half of the aperture wall, and the photograph shows no evidence of carbon deposition in this part of the aperture. At the end of the test though, the current density distribution has shifted downstream as a result of the geometry changes and net erosion occurs only at the very end of the aperture and on the walls of the carbon deposits. This is consistent with the photograph, which shows thick deposits on the aperture walls. In these analyses we also varied the carbon sputter yield over the range of the 50% likelihood fit from Yim's analysis of sputter yield data [29] and found the same qualitative trends, so the conclusions are robust to uncertainty in this parameter.

The results of the analyses for all of the test segments are summarized in Fig. 17. The photographs of the center aperture show the evolution of the carbon deposits on the hole wall. At 6,114 hours there was still net erosion, as shown in the first photo. However, by the end of the segment the hole enlargement resulted in a reduction in charge exchange ion current density and energy and a much lower erosion rate. In addition, growth of downstream carbon deposits shifted the impingement current distribution further downstream, resulting in net erosion only at the downstream end of the aperture. This appears to be consistent with the photograph at 13,033 hours. The modeling indicates that segments 2 through 5 should experience net erosion at a very low rate or net deposition, although also at a low rate. The impingement current densities and energies at these throttled conditions are lower, but the carbon backsputter rates are also lower. The photographs from these test segments appear to show metal surfaces or thin carbon deposits, which is consistent with the modeling. The simulations indicate that the aperture wall in the final TL40 test segment should not suffer significant erosion because of aperture enlargement due to operation at the previous throttle levels. Instead,

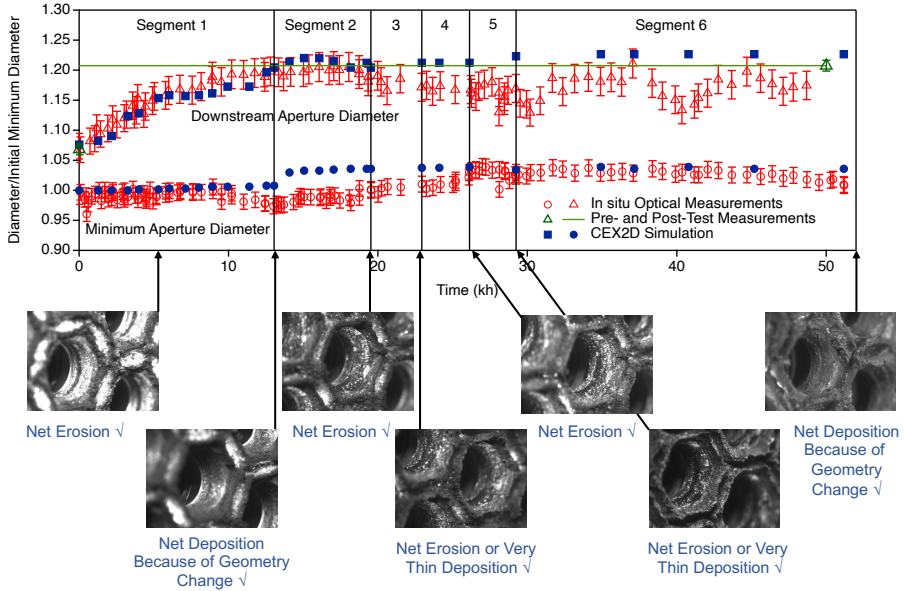


Fig. 17 Predictions of aperture diameter compared to measurements for the NEXT LDT. The photos indicate conditions of net erosion or net deposition. Check marks indicate that the simulations agreed with observations.

it experienced net deposition over most of the axial extent of the hole wall because of the combined effect of the aperture enlargement and the thick downstream deposits on the impingement current distribution, as shown in Fig. 16.

The measured and calculated hole diameters are plotted above the photos in Fig. 17. The CEX2D code accurately captures the erosion over the first test segment and the fact that there is essentially no erosion during the next four segments. The agreement between the erosion measurements and predictions and the observations of net deposition at some operating points provide further confidence in the charge exchange ion models and the erosion models.

4 Assessment of NEXT Life in Space

After validating the codes over a range of conditions, we used them to assess the lifetime and throughput limitations due to screen grid failure and electron backstreaming for NEXT operated at points spanning the throttle range (TL1, 5, 12, 37, and 40) in space. These two failure modes are important in different parts of the throttling range. Screen grid erosion is not a dominant failure mode for the higher throttle levels, but appears to be the first failure mode for the lowest throttle levels. In contrast, electron backstreaming is not important

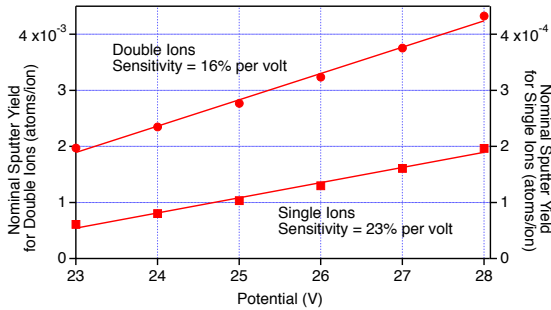


Fig. 18 Sensitivity of screen grid sputter yield to upstream plasma potential for double and single ions.

for the lower throttle levels, but is the first failure mode at the highest throttle levels.

4.1 Input Parameters

For these simulations the grid thicknesses, beam radius, and grid radius of curvature were based on the nominal specification, while the aperture geometries were based on pre- and post-test measurements of the grids used in the NEXT LDT. The hot grid gap was the same used in the NEXT LDT simulations, which were based on Herman’s optical measurements [36]. The beam and accelerator grid voltages were set equal to the nominal throttle table values.

The discharge voltages were based on measurements from the PM1R thruster [42]. For throttle levels TL37 and TL40, these voltages were very similar to those measured in the LDT, but for the lower throttle levels the discharge voltage was 1 to 1.5 V higher than in the LDT. The discharge voltage was treated as constant in time. However, it is often observed to increase in time during wear tests, largely due to accelerator grid aperture erosion, cathode orifice erosion, and minor changes in thermal characteristics [53–55]. In the NEXT LDT the discharge voltage increased by 1 to 2 V, depending on the throttle level. These differences are unimportant for accelerator grid aperture erosion, but can have a significant impact on screen grid erosion, where the ion impact energies are close to the sputtering threshold and the yield is a steep function of energy. As shown in Fig. 18, the yield for single ions increases 23% per volt and that for double ions increases 16% per volt in the range of 23 - 28 V. The throttle levels most susceptible to screen erosion don’t have much accelerator grid aperture or cathode orifice erosion, so the discharge voltage is not likely to increase much during extended operation at a low throttle level. However, missions with extended operation at high power (which experience significant hole erosion) followed by low power operation at an elevated discharge voltage may suffer greater screen grid erosion than predicted here. These cases should be investigated in more detail for particular throttling profiles.

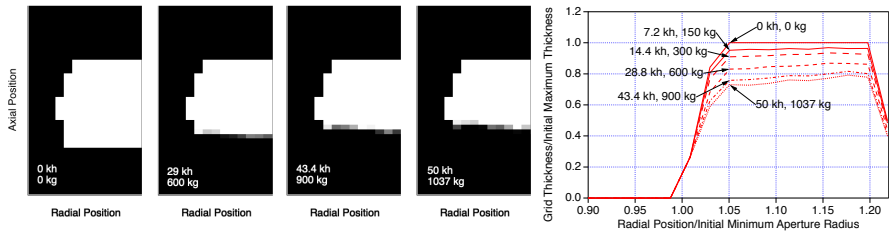


Fig. 19 Predicted screen grid erosion as a function of time and throughput for operation in space at TL40.

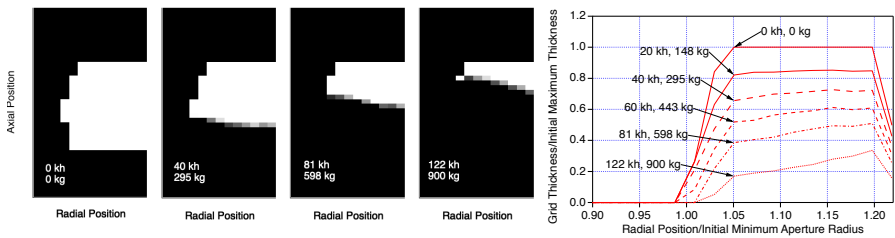


Fig. 20 Predicted screen grid erosion as a function of time and throughput for operation in space at TL5.

The beamlet currents and double ion current fractions in these simulations were based on Faraday probe and ExB probe measurements, respectively, in the beam of the PM1R thruster [42]. For the upstream and downstream plasma potential and electron temperature and the neutral gas parameters we used the same values as in the NEXT LDT simulations. The ambient pressure was set to zero to simulate space conditions. For the sputter yields we used the maximum likelihood estimates from Yim's fits to data [29] for the screen grid erosion and the lower boundary of the 50% likelihood estimate for the hole wall erosion.

4.2 Screen Grid Structural Failure

At some point, thinning of the screen grid due to erosion will cause a structural failure. Prior to that, however, screen grid thinning will likely reduce the strength of the grid enough that it will deflect under the electrostatic load between the grids, resulting in a smaller grid gap. A structural analysis of the screen grid deflection due to electrostatic forces as a function of screen grid thickness shows minimal displacement down to about 25% of the original thickness, so that was used as the failure criterion. Screen grids have experienced significant erosion in wear tests without actual failure [56], so this failure criterion is likely conservative.

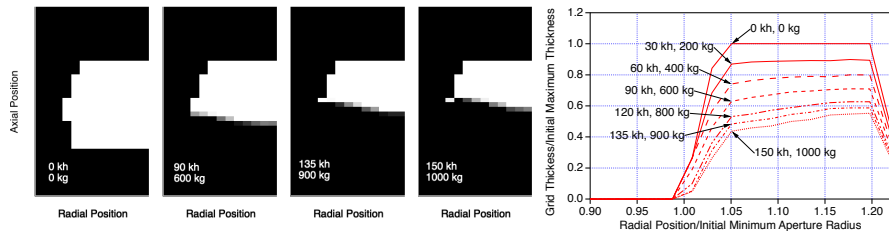


Fig. 21 Predicted screen grid erosion as a function of time and throughput for operation in space at TL1.

The screen erosion for operation at the peak power (TL40) is shown in Fig. 19. The images on the left are the screen grid cross sections at four different times. The grid thickness as a function of time and radial position is shown on the right. Even after 50,000 hours of operation, in which over 1000 kg of propellant is consumed, the grid has lost only about 25% of its original thickness. In this case, screen erosion is not the dominant failure mode.

The worst case condition is TL5. The results for this low power condition plotted in Fig. 20 show that it reaches a thickness of 25% after about 122,000 hours, after processing 900 kg of xenon. In this case, low voltage operation leads to poor transparency, as shown in Fig. 8. Even though the beam current is over three times lower, the screen grid current is nearly as high as at full power. The rate at which propellant is processed is proportional to the beam current, so at this operating point the amount of screen grid erosion experienced per kg of propellant consumed is much larger. This is exacerbated by the fact that the discharge voltage at TL5 is about three volts higher than at TL40.

The lowest power level (TL1) is an intermediate case, as the results plotted in Fig. 21 show. About 50% of the grid remains after 150,000 hours and 1000 kg. However, it is unlikely that the thruster would be operated this long at this low power operating point. In addition, the comparisons with NSTAR and NEXT data presented above show that the model tends to overestimate the screen erosion, so these results are likely conservative.

4.3 Electron Backstreaming

Failure in this case is taken to be the point at which the nominal accelerator grid voltage can no longer prevent electron backstreaming for the eroded geometry. Simulations at the low throttle levels show very low erosion rates, so electron backstreaming is not a credible failure mode.

Figure 22 shows the accelerator grid cross sections at several times and the resulting change in the electron backstreaming voltage as a function of time at TL37. The model predicts minimal erosion of the upstream hole edge, the formation of a notch in the hole wall due to charge exchange ion focusing into that region, and chamfering of the downstream hole edge. CEX2D does not

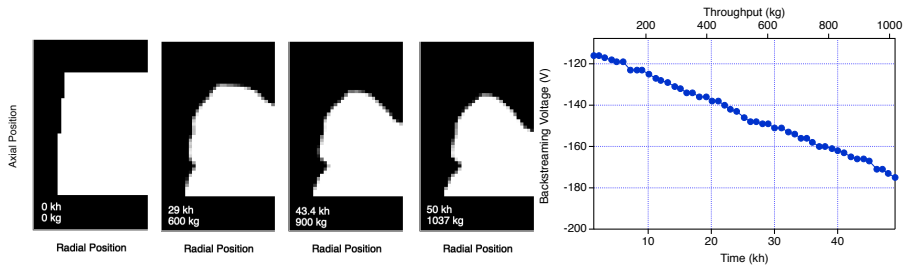


Fig. 22 Predicted accelerator grid aperture erosion and electron backstreaming voltage for operation in space at TL37.

accurately model the inherently three-dimensional pits and grooves erosion pattern that forms on the downstream surface, so the downstream features should be ignored. The nominal accelerator grid voltage at TL37 is -200 V, so even after 50,000 hours and more than 1000 kg of xenon throughput, the accelerator grid still has about 25 V margin. Even with the uncertainty of ± 15 V in predicted voltages compared to measurements that was found in comparisons with NSTAR and NEXT ground test data, the engine should not experience failure due to backstreaming in this period.

The change in the backstreaming limit as a function of operating time for TL40 is shown in Fig. 23. In this case, the nominal accelerator grid voltage is -210 V, so the model predicts failure after greater than 50,000 hours and over 1000 kg of xenon throughput. However, with the ± 15 V model uncertainty, failure could occur at as low as 700 kg throughput. The thruster life could be extended by increasing the magnitude of the accelerator grid voltage at some point during the mission to provide more margin against backstreaming. This comes at the expense of increased erosion rates, but significant gains in throughput can be achieved with modest changes in accelerator grid voltage.

5 Summary and Conclusions

The ion optics erosion codes CEX2D and CEX3D were employed to assess the lifetime limits of NEXT in space due to screen grid and accelerator grid aperture erosion over a range of operating conditions that span the throttle table. The code inputs for the deterministic analysis were nominal values based primarily on measurements from high fidelity hardware that are representative of what would be expected in flight operation. The greatest uncertainty is in the hot grid gap, which influences the ion focusing, the neutral density distribution upstream of the grids, which is a primary driver of charge exchange ion formation and strongly influences accelerator grid erosion, and the sputter yield variation with energy and incidence angle, which affects erosion of both grids. Measurements of the hot grid gap in NEXT were used for those simulations, but in some validation cases we had to infer the grid gap by matching electron

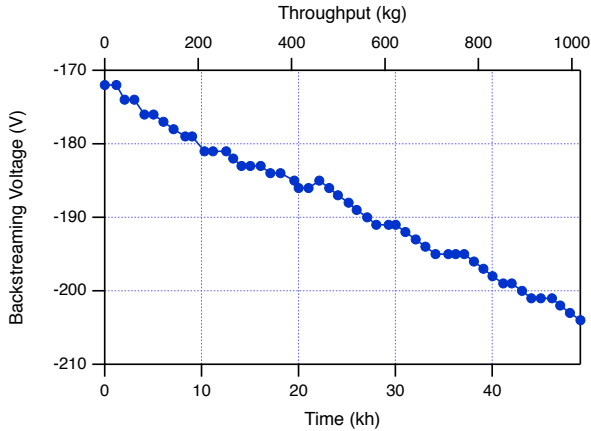


Fig. 23 Electron backstreaming voltage as a function of time and throughput for operation in space at TL40.

backstreaming voltage at beginning of life or downstream accelerator grid erosion patterns. The neutral density was assumed to be uniform and equal an average value that is consistent with the total neutral flow from the engine. The sputter yield in the range of energies relevant for accelerator grid erosion was assumed to be at the low end of experimental measurements. These assumptions led to good agreement with measured accelerator grid aperture erosion for two different thrusters and a wide range of operating conditions, although similarly good agreement may be achieved with different combinations of these parameters. For sputtering at energies near threshold we assumed the nominal yield based on sparse measurements in this energy range. Further measurements of yield and neutral density distribution should be made to reduce the uncertainty in these parameters.

The screen grid erosion models were validated by measurements of screen grid transparency and grid erosion rates in wear tests of the NSTAR engines and NEXT. Comparisons of measured and calculated screen grid current showed good agreement, demonstrating that the models of the primary ion impingement are accurate. However, the calculated values of screen grid erosion were generally two to three times higher than measured values, suggesting that the actual sputter yield near threshold is lower than current data and semi-empirical curve fits would suggest. The accelerator grid erosion models were validated with measurements of electron backstreaming voltage and aperture enlargement in NSTAR and NEXT wear tests. The calculated electron backstreaming voltage for well-characterized beginning of life grid geometries agreed with measurements to within ± 15 V and the difference was correlated with the perveance fraction, suggesting some model error in the charge density or potential calculation. The agreement between measured and calculated grid erosion was excellent for both NSTAR and NEXT.

The codes were also used to assess the impact that carbon deposits on the accelerator grid had on the aperture erosion rates in the NEXT LDT. Using a model that predicts the current density at which the transition between net erosion and net deposition occurs, we predicted the conditions under which carbon should accumulate on the aperture walls. These predictions agreed well with observations, providing another demonstration that the models accurately reproduce the flux and energy of charge exchange ions striking the hole walls. Combining these results with predictions of aperture erosion, we concluded that the carbon deposits prevented erosion that otherwise would have occurred in the final test segment at full power. However, the calculated erosion agreed well with the observed aperture enlargement from the first segment, which experienced net carbon deposition only at the very end. The subsequent low power operating points from the throttle profile test suffered little or no carbon deposition, but were not subject to significant aperture erosion anyway. Although the wear characteristics of some portions of the NEXT LDT were not representative of operation in space due to carbon backspattering, it still provided a wealth of data that helped validate the erosion models.

The validated codes were then used to predict the time to failure in space due to screen grid structural failure or electron backstreaming. We found that screen grid erosion was only important at low throttle levels, leading to failure after processing 900 kg of propellant at TL5, or over 1000 kg at TL1. As noted above, the code tends to overpredict screen grid erosion rates by a factor of two to three, so these results are likely quite conservative. In addition, it is unlikely that this amount of propellant would be processed at these low throttle levels. This erosion could also be mitigated to a large extent by operating at conditions with better transparency and at flow rates that reduce the discharge voltage by a volt or two.

Accelerator grid erosion ultimately leading to electron backstreaming was found to be the dominant failure mode at high power levels. Electron backstreaming would occur after processing more than 1000 kg of xenon at TL37 and after about 700 kg for TL40, even with margin added to accommodate the ± 15 V error in calculated backstreaming voltage. The simulations of accelerator grid structural failure due to erosion in the pits and grooves pattern on the downstream grid face [13] yielded predicted time to failure that was greater than that for electron backstreaming. These simulations were more difficult to validate, but generally predicted higher erosion rates than those observed, so these results are likely conservative. Therefore, backstreaming due to hole wall erosion is the first failure mechanism. If necessary, electron backstreaming at a given operating point could be delayed by increasing the accelerator grid voltage during the mission.

6 Declarations

Funding. The research described in this paper was carried out in part at the Jet Propulsion Laboratory, California Institute of Technology, under a contract with the National Aeronautics and Space Administration.

Conflicts of interest/Competing interests. The authors declare that they have no known competing financial interests or personal relationships that could have influenced the work reported in this paper.

Data availability. Data are available upon reasonable request to the authors.

Code availability. The CEX2D and CEX3D codes may be licensed from the Jet Propulsion Laboratory, California Institute of Technology, subject to ITAR restrictions.

Authors' contributions. All authors contributed to the research. Simulations were conducted by James Polk and Vernon Chaplin. Modifications to the codes as part of this work were done by Vernon Chaplin with contributions from James Polk. Other coauthors provided input and validation data, reviewed the results, and offered valuable insights and suggestions.

References

- [1] Shastry, R., Soulas, G., Aulisio, M., Schmidt, G.: Current Status of NASA's NEXT-C Ion Propulsion System Development Project. Paper IAC-17.C4.4.3, presented at the 68th International Astronautical Congress, Adelaide, Australia, 25–29 September 2017 (2017)
- [2] Herman, D.A.: NEXT Long-Duration Test Neutralizer Performance and Erosion Characteristics. Paper IEPC-2009-154, presented at the 31st International Electric Propulsion Conference, Ann Arbor, Michigan, 20–24 September, 2009 (2009)
- [3] Brophy, J., Polk, J., Randolph, T.: Lifetime Qualification Standards for Electric Thrusters for Deep-Space Missions. Paper AIAA-2008-5184, presented at the 44th AIAA/ASME/SAE/ASEE Joint Propulsion Conference, Hartford, Connecticut, 21–23 July, 2008 (2008). <https://doi.org/10.2514/6.2008-5184>
- [4] Dankanich, J.W., Brophy, J.R., Polk, J.E.: Lifetime Qualification Standard for Electric Thrusters. Paper AIAA 2009-5095, presented at the 45th AIAA/ASME/SAE/ASEE Joint Propulsion Conference, Denver, Colorado, 2–5 August, 2009 (2009). <https://doi.org/10.2514/6.2009-5095>
- [5] Patterson, M.J., Benson, S.W.: NEXT Ion Propulsion System Development Status and Performance. Paper AIAA-2007-5199, presented at the

- 43rd AIAA/ASME/SAE/ASEE Joint Propulsion Conference, Cincinnati, Ohio, 8–11 July, 2007 (2007). <https://doi.org/10.2514/6.2007-5199>
- [6] Soulas, G.C., Patterson, M.J.: NEXT Ion Thruster Performance Dispersion Analyses. Paper AIAA-2007-5213, presented at the 43rd AIAA/ASME/SAE/ASEE Joint Propulsion Conference, Cincinnati, Ohio, 8–11 July, 2007 (2007). <https://doi.org/10.2514/6.2007-5213>
- [7] Frandina, M.M., Arrington, L.A., Soulas, G.C., Hickman, T.A., Patterson, M.J.: Status of the NEXT Ion Thruster Long Duration Test. Paper AIAA-2005-4065, presented at the 41st AIAA/ASME/SAE/ASEE Joint Propulsion Conference, Tucson, Arizona, 10–13 July, 2005 (2005). <https://doi.org/10.2514/6.2005-4065>
- [8] Herman, D.A., Soulas, G.C., Patterson, M.J.: Performance Characteristics of the NEXT Long-Duration Test after 16,550 h and 337 kg of Xenon Processed. Paper AIAA-2008-4527, presented at the 44th AIAA/ASME/SAE/ASEE Joint Propulsion Conference, Hartford, Connecticut, 21–23 July, 2008 (2008). <https://doi.org/10.2514/6.2008-4527>
- [9] Patterson, M.J., Foster, J.E., Haag, T.W., Rawlin, V.K., Soulas, G.C., Roman, R.F.: NEXT: NASA’s Evolutionary Xenon Thruster. Paper AIAA-2002-3832, presented at the 38th AIAA/ASME/SAE/ASEE Joint Propulsion Conference, Indianapolis, Indiana, 7–10 July, 2002 (2002). <https://doi.org/10.2514/6.2002-3832>
- [10] Soulas, G.C., Domonkos, M.T., Patterson, M.J.: Performance Evaluation of the NEXT Ion Engine. Paper AIAA-2003-5278, presented at the 39th AIAA/ASME/SAE/ASEE Joint Propulsion Conference, Huntsville, Alabama, 20–23 July, 2003 (2003). <https://doi.org/10.2514/6.2003-5278>
- [11] Herman, D.A.: Status of the NASA’s Evolutionary Xenon Thruster (NEXT) Long-Duration Test after 30,352 Hours of Operation. Paper AIAA-2010-7112, presented at the 46th AIAA/ASME/SAE/ASEE Joint Propulsion Conference, Nashville, Tennessee, 25–28 July, 2010 (2010). <https://doi.org/10.2514/6.2010-7112>
- [12] Shastry, R., Herman, D.A., Soulas, G.C., Patterson, M.J.: End-of-test Performance and Wear Characterization of NASA’s Evolutionary Xenon Thruster (NEXT) Long-Duration Test. Paper AIAA 2014-3617, presented at the 50th AIAA/ASME/SAE/ASEE Joint Propulsion Conference, Cleveland, Ohio, 28–30 July, 2014 (2014). <https://doi.org/10.2514/6.2014-3617>
- [13] Chaplin, V.H., Polk, J.E., Katz, I., Anderson, J.R., Williams, G.J., Soulas, G.C., Yim, J.T.: 3d simulations of ion thruster accelerator grid erosion accounting for charge exchange ion space charge. Paper AIAA-2018-4812

- presented at the 54th AIAA/ASME/SAE/ASEE Joint Propulsion Conference, Cincinnati, Ohio, 9–11 July, 2018 (2018). <https://doi.org/10.2514/6.2018-4812>
- [14] Yim, J.T., Williams, G.J., Shastry, G.C. R. and Soulas, Chaplin, V.H., Polk, J.E.: Uncertainty Quantification of Modeled Electron Backstreaming Failure for the NEXT Ion Thruster. Paper IEPC-2019-722, presented at the 36th International Electric Propulsion Conference, University of Vienna, Austria, 15–20 September, 2019 (2019)
- [15] Wirz, R.E., Katz, I., Goebel, D.M., Anderson, J.R.: Electron Backstreaming Determination for Ion Thrusters. *Journal of Propulsion and Power* **27**(1), 206–210 (2011). <https://doi.org/10.2514/1.46844>
- [16] Wirz, R.E., Anderson, J.R., Katz, I.: Time-Dependent Erosion of Ion Optics. *Journal of Propulsion and Power* **27**(1), 211–217 (2011). <https://doi.org/10.2514/1.46845>
- [17] Anderson, J.R., Katz, I., Goebel, D.M.: Numerical Simulation of Two-Grid Ion Optics Using a 3D Code. Paper AIAA-2004-3782, presented at the 40th AIAA/ASME/SAE/ASEE Joint Propulsion Conference, Ft. Lauderdale, Florida, 11–14 July, 2004 (2004). <https://doi.org/10.2514/6.2004-3782>
- [18] Nakano, M.: Three-dimensional simulations of grid erosion in ion engines. *Vacuum* **83**(1), 82–85 (2008). <https://doi.org/10.1016/j.vacuum.2008.03.080>
- [19] Shagayda, A., Nikitin, V., Tomilin, D.: Three-dimensional analysis of ion optics with misalignments of apertures. *Vacuum* **123**, 140–150 (2016). <https://doi.org/10.1016/j.vacuum.2015.10.030>
- [20] Kuzmin, A., Luisier, M., Schenk, O.: Fast methods for computing selected elements of the greens function in massively parallel nanoelectronic device simulations. In: Wolf, F., Mohr, B., Mey, D. (eds.) *Euro-Par 2013 Parallel Processing*, Lecture Notes in Computer Science vol. 8097, pp. 533–544. Springer, Berlin Heidelberg (2013). https://doi.org/10.1007/978-3-642-40047-6_54
- [21] Schenk, O., Gärtner, K.: Solving Unsymmetric Sparse Systems of Linear Equations with PARDISO. *Journal of Future Generation Computer Systems* **20**(3), 475–487 (2004)
- [22] Mikellides, I.G., Jongeward, G.A., Katz, I., Manzella, D.H.: Plume Modeling of Stationary Plasma Thrusters and Interactions with the Express-A Spacecraft. *Journal of Spacecraft and Rockets* **39**(6), 894–903 (2002). <https://doi.org/10.2514/2.3896>

- [23] Miller, J.S., Pullins, S.H., Levandier, D.J., Chiu, Y., Dressler, R.A.: Xenon charge exchange cross sections for electrostatic thruster models. *J. Appl. Phys* **91**(3), 984–991 (2002). <https://doi.org/10.1063/1.1426246>
- [24] Birdsall, C.K., Langdon, A.B.: *Plasma Physics Via Computer Simulation*, Series in Plasma Physics. Taylor and Francis, Boca Raton, FL (2004)
- [25] Araki, S.J., Wirz, R.E.: Ion-neutral collision modeling using classical scattering with spin-orbit free interaction potential. *IEEE Transactions on Plasma Science* **41**(3), 470–480 (2013). <https://doi.org/10.1109/TPS.2013.2241457>
- [26] Araki, S.J., Wirz, R.E.: Modeling of Elastic Collisions between High Energy Ions and Slow Neutral Atoms. Paper IEPC-2015-202, presented at the 34th International Electric Propulsion Conference, Hyogo-Kobe, Japan 4–10 July, 2015 (2015)
- [27] Patino, M.I., Wirz, R.E.: Characterization of Xenon Ion and Neutral Interactions in a Well-Characterized Experiment. *Phys. Plasmas* **25**, 062108 (2018). <https://doi.org/10.1063/1.5030464>
- [28] Eckstein, W.: New Fit Formulae for the Sputtering Yield. *Journal of Nuclear Materials* **329**, 209–213 (2003). [https://doi.org/10.1016/S0022-3115\(03\)00192-2](https://doi.org/10.1016/S0022-3115(03)00192-2)
- [29] Yim, J.T.: A survey of xenon ion sputter yield data and fits relevant to electric propulsion spacecraft integration. Paper IEPC-2017-060, presented at the 35th International Electric Propulsion Conference, Georgia Institute of Technology, Atlanta, Georgia, 8–12 October, 2017 (2017)
- [30] Wei, Q., Li, K., Lian, J., Wang, L.: Angular Dependence of Sputtering Yield of Amorphous and Polycrystalline Materials. *J. Phys. D: Appl. Phys.* **41**, 172002 (2008). <https://doi.org/10.1088/0022-3727/41/17/172002>
- [31] Farnell, C.C.: *Performance and Lifetime Simulation of Ion Thruster Optics*. PhD, Colorado State University (2007)
- [32] Yalin, A.P., Williams, J.D., Surla, V., Zoerb, K.A.: Differential sputter yield profiles of molybdenum due to bombardment by low energy xenon ions at normal and oblique incidence. *Journal of Physics D: Applied Physics* **40**, 3194–3202 (2011). <https://doi.org/10.1088/0022-3727/40/10/025>
- [33] Polk, J.E., Anderson, J.R., Brophy, J.R., Rawlin, V.K., Patterson, M.J., Sovey, J., Hamley, J.: An Overview of the Results from an 8200 Hour Wear Test of the NSTAR Ion Thruster. Paper AIAA 99-2446, presented

- at the 35th AIAA/ASME/SAE/ASEE Joint Propulsion Conference, Los Angeles, California, 20–24 June, 1999 (1999). <https://doi.org/10.2514/6.1999-2446>
- [34] Anderson, J.R., Sengupta, A., Brophy, J.R.: Post-Test Analysis of the Deep Space One Spare Flight Thruster Ion Optics. Paper AIAA-2004-3010, presented at the 40th AIAA/ASME/SAE/ASEE Joint Propulsion Conference, Ft. Lauderdale, Florida, 11–14 July, 2004 (2004). <https://doi.org/10.2514/6.2004-3010>
- [35] Diaz, E.M., Soulas, G.C.: Grid Gap Measurement for an NSTAR Ion Thruster. Paper IEPC-2005-244 presented at the 29th International Electric Propulsion Conference, Princeton University, Princeton, New Jersey, 31 October–4 November, 2005 (2005)
- [36] Herman, D.A., Patterson, M.J., Soulas, G.C.: NASA’s Evolutionary Xenon Thruster (NEXT) Prototype-Model Ion Optics Operating Grid-Gap Measurements. Paper presented at the 68th JANNAF Propulsion Meeting, Orlando, Florida, 8–12 December, 2008 (2008)
- [37] Brophy, J.R.: Propellant Throughput Capability of the Dawn Ion Thrusters. Paper IEPC-2007-279, presented at the 30th International Electric Propulsion Conference, Florence, Italy, 17–20 September, 2007 (2007)
- [38] Sengupta, A., Brophy, J.R., Goodfellow, K.D.: Status of the Extended Life Test of the Deep Space 1 Flight Spare Ion Engine After 30,352 Hours of Operation. Paper AIAA-2003-4558, presented at the 39th AIAA/ASME/SAE/ASEE Joint Propulsion Conference, Huntsville, Alabama, 20–23 July, 2003 (2003). <https://doi.org/10.2514/6.2003-4558>
- [39] Kamhawi, H., Soulas, G., Patterson, M., Frandina, M.: NEXT Ion Engine 2000 Hour Wear Test Plume and Erosion Results. Paper AIAA-2004-3791, presented at the 40th AIAA/ASME/SAE/ASEE Joint Propulsion Conference, Ft. Lauderdale, Florida, 11–14 July, 2004 (2004). <https://doi.org/10.2514/6.2004-3791>
- [40] Sengupta, A., Goebel, D.M., Owens, A.G.: Langmuir Probe Studies of Magnetic Confinement in an Ion Thruster Discharge Plasma. *J. Propul. Power* **25**(2), 387–396 (2009). <https://doi.org/10.2514/1.36547>
- [41] Herman, D.A.: The Use of Electrostatic Probes to Characterize the Discharge Plasma Structure and Identify Discharge Cathode Erosion Mechanisms in Ring-Cusp Ion Thrusters. PhD, University of Michigan (2005)
- [42] Pollard, J.E., Diamant, K.D., Crofton, M.W., Patterson, M.J., Soulas,

- G.C.: Spatially-Resolved Beam Current and Charge-State Distributions for the NEXT Ion Engine. Paper AIAA 2010-6779, presented at the 46th AIAA/ASME/SAE/ASEE Joint Propulsion Conference, Nashville, Tennessee, 25–28 July, 2010 (2010). <https://doi.org/10.2514/6.2010-6779>
- [43] Foster, J.E., Patterson, M.J., Pencil, E., McEwen, H., Diaz, E.: Plasma Characteristics Measured in the Plume of a NEXT Multi-Thruster Array. Paper AIAA 2006-5181, presented at the 42nd AIAA/ASME/SAE/ASEE Joint Propulsion Conference, Sacramento, California, 9–12 July, 2006 (2006). <https://doi.org/10.2514/6.2006-5181>
- [44] Brinza, D., Mactutis, A.T., McCarty, K.P., Rademacher, J.D., van Zandt, T.R., Narvaez, P., Wang, J.J., Tsurutani, B.T., Katz, I., Davis, V.A., Moses, S., Musmann, G., Kuhnke, F., Richter, I., Othmer, C., Glassmeier, K.H., Henty, M.D.: Plasma Characteristics Measured in the Plume of a NEXT Multi-Thruster Array. Paper AIAA 2001-0966, presented at the 39th AIAA Aerospace Sciences Meeting, Reno, Nevada, 8–11 January, 2001 (2001). <https://doi.org/10.2514/6.2001-966>
- [45] Sengupta, A., Goebel, D., Fitzgerald, D., Owens, A., Tynan, G., Doerner, R.: Experimentally Determined Neutral Density and Plasma Parameters in a 30cm Ion Engine. Paper AIAA-2004-3613, presented at the 40th AIAA/ASME/SAE/ASEE Joint Propulsion Conference, Ft. Lauderdale, Florida, 11–14 July, 2004 (2004). <https://doi.org/10.2514/6.2004-3613>
- [46] Wirz, R., Katz, I.: Plasma Processes of DC Ion Thruster Discharge Chambers. Paper AIAA-2005-3690, presented at the 41st AIAA/ASME/SAE/ASEE Joint Propulsion Conference, Cincinnati, Ohio, 10–13 July, 2005 (2005). <https://doi.org/10.2514/6.2005-3690>
- [47] Rawlin, V.K., Patterson, M.J., Becker, R.A.: Thermal Environmental Testing of NSTAR Engineering Model Ion Thrusters. Paper IEPC-97-051, presented at the 25th International Electric Propulsion Conference, Cleveland, Ohio, 24–28 August, 1997 (1997)
- [48] Anderson, J.R., Snyder, J.S., Van Noord, J.L., Soulas, G.C.: Thermal Development Test of the NEXT PM1 Ion Engine. Paper AIAA-2007-5217, presented at the 43rd AIAA/ASME/SAE/ASEE Joint Propulsion Conference, Cincinnati, Ohio, 8–11 July, 2007 (2007). <https://doi.org/10.2514/6.2007-5217>
- [49] Bird, G.A.: *Molecular Gas Dynamics and the Direct Simulation of Gas Flows*. Clarendon Press, Oxford (1994)
- [50] LeBeau, G.J., Lumpkin, F.E.: Application highlights of the DSMC analysis code (DAC) software for simulating rarefied flows. *Computer Methods in Applied Mechanics and Engineering* **191**(6-7), 595–609 (2001). [https://doi.org/10.1016/S0045-7825\(01\)00101-1](https://doi.org/10.1016/S0045-7825(01)00101-1)

[//doi.org/10.1016/S0045-7825\(01\)00304-8](https://doi.org/10.1016/S0045-7825(01)00304-8)

- [51] Soulas, G.C.: Design and Performance of 40 cm Ion Optics. Paper IEPC-01-090, presented at the 31st International Electric Propulsion Conference, Pasadena, California, 15–19 October, 2001 (2001)
- [52] Soulas, G.C.: The Impact of Back-Sputtered Carbon on the Accelerator Grid Wear Rates of the NEXT and NSTAR Ion Thrusters. Paper IEPC-2013-157, presented at the 33rd International Electric Propulsion Conference, The George Washington University, Washington, D.C., 6–10 October, 2013 (2013)
- [53] Polk, J.E., Anderson, J.R., Brophy, J.R., Rawlin, V.K., Patterson, M.J., Sovey, J.S.: The Effect of Engine Wear on Performance in the NSTAR 8000 Hour Ion Engine Endurance Test. Paper AIAA-97-3387, presented at the 33rd AIAA/ASME/SAE/ASEE Joint Propulsion Conference, Seattle, Washington, 6–9 July, 1997 (1997). <https://doi.org/10.2514/6.1997-3387>
- [54] Goebel, D.G., Polk, J.E., Mikellides, I.G.: Ion Thruster Performance Impacts Due to Cathode Wear. *Journal of Propulsion and Power* **27**(4), 728 (2011). <https://doi.org/10.2514/1.55011>
- [55] Van Noord, J.L., Soulas, G.C., Sovey, J.S.: NEXT PM1R Ion Thruster and Propellant Management System Wear Test Results. Paper IEPC-2009-163, presented at the 31st International Electric Propulsion Conference, Ann Arbor, Michigan, 20–24 September, 2009 (2009)
- [56] Tighe, W.G., Chien, K.-r., Solis, Z., Spears, R.: The 25 cm XIPS © Life Test and Post-Test Analysis. Paper IEPC-2009-161, presented at the 31st International Electric Propulsion Conference, Ann Arbor, Michigan, 20–24 September, 2009 (2009)

Appendix A Sources of Data for Model Inputs

The codes require the parameters listed in the first column of Table A1 as inputs. These are organized under the categories of optics geometry, the potentials applied to the thruster components, plasma properties in the discharge chamber and the beam, and the neutral gas properties. The sources of data used to define these parameters for each of the tests used in model validation are summarized in the table.

Table A1 Sources of data used to define CEX2D and CEX3D code input parameters

Parameter	NSTAR 8200 Hour LDT	NSTAR 30,352 Hour ELT	NEXT 2000 Hour Test	NEXT 51,184 Hour LDT	NEXT Space Conditions
Geometry					
<i>Screen Grid Thickness</i>	Post-test SEM measurements [33]	Specification, corrected for stretching during dishing [34]	Specification	Pre-test measurements at edge, post-test SEM measurements corrected for erosion and thinning due to dishing	Specification
<i>Accelerator Grid Thickness</i>	Post-test SEM measurements [33]	Specification	Specification	Post-test SEM measurements	Specification
<i>Screen Aperture Geometry</i>	Post-test measurements [33]	Specification (minimum hole diameter), post-test SEM measurements (upstream and downstream diameters) [34]	Pre-test pin measurements (minimum hole diam), post-test measurements (upstream and downstream diameters)	Pre-test pin measurements (minimum hole diam), post-test measurements (upstream and downstream diameters)	Specification (minimum hole diam), NEXT LDT post-test measurements (upstream and downstream diameters)
<i>Accelerator Aperture Geometry</i>	Specification (minimum hole diameter), post-test measurements (upstream and downstream diameters) [33]	Pre-test pin measurements (minimum hole diam), post-test SEM measurements (upstream and downstream diameters) [34]	Pre-test pin measurements (minimum hole diam), post-test measurements (upstream and downstream diameters)	Pre-test pin and putty measurements	Specification (minimum hole diam), NEXT LDT pre-test measurements (upstream and downstream diameters)
<i>Grid Gap</i>	Inferred from BOL electron backstreaming simulations	Assumed to be the same as the NSTAR LDT grids	Inferred from characteristics of erosion pattern	Optical measurements of hot grid gap [36]	Optical measurements of hot grid gap [36]
<i>Optics Radius of Curvature</i>	Specification	Specification	Specification	Specification	Specification
<i>Beam Radius</i>	Specification	Specification	Specification	Specification	Specification
Electrical Parameters					
<i>Beam Voltage</i>	Nominal voltage from throttle table [33]	Nominal voltage from throttle table [38]	Nominal voltage from throttle table [39]	Nominal voltage from throttle table [12]	Nominal voltage from throttle table [12]
<i>Discharge Voltage</i>	Average values from each segment measured at the thruster [33]	Average values from each segment measured at the thruster [38]	BOL values measured at the thruster [39]	BOL values measured at the thruster [12]	Measurements on PMIR thruster [42]
<i>Accelerator Grid Voltage</i>	Nominal voltage from throttle table [33]	Nominal voltage from throttle table [38]	Nominal voltage from throttle table [39]	Nominal voltage from throttle table [12]	Nominal voltage from throttle table [12]

Table A1 Sources of data used to define CEX2D and CEX3D code input parameters (continued)

Parameter	NSTAR 8200 Hour LDT	NSTAR 30,352 Hour ELT	NEXT 2000 Hour Test	NEXT 51,184 Hour LDT	NEXT Space Conditions
Upstream Plasma Properties					
<i>Beamlet Current</i>	Faraday probe measurements, extrapolated back to grid [37]	Faraday probe measurements, extrapolated back to grid [15, 37, 38]	Faraday probe measurements, extrapolated back to grid [39]	Measurements at 3.52 and 1.2 A extrapolated to grid; 1.0 A scaled from 1.2 A data [12]	Faraday probe measurements on PMIR thruster [42]
<i>Plasma Density</i>	Determined iteratively from jb in CEX2D; these values then used in CEX3D	Determined iteratively from jb in CEX2D; these values then used in CEX3D	Determined iteratively from jb in CEX2D; these values then used in CEX3D	Determined iteratively from jb in CEX2D; these values then used in CEX3D	Determined iteratively from jb in CEX2D; these values then used in CEX3D
<i>Plasma Potential</i>	Assumed equal to discharge voltage (consistent with emissive probe measurements on LM thruster) [40]	Assumed equal to discharge voltage (consistent with emissive probe measurements on LM thruster) [40]	Assumed equal to discharge voltage (consistent with emissive probe measurements on LM thruster) [41]	Assumed equal to discharge voltage (consistent with emissive probe measurements on LM thruster) [41]	Assumed equal to discharge voltage (consistent with emissive probe measurements on LM thruster) [41]
<i>Electron Temperature</i>	5 eV for all cases (consistent with Langmuir probe measurements on LM thruster) [40]	5 eV for all cases (consistent with Langmuir probe measurements on LM thruster) [40]	5 eV for all cases (consistent with Langmuir probe measurements on LM thruster) [41]	5 eV for all cases (consistent with Langmuir probe measurements on LM thruster) [41]	5 eV for all cases (consistent with Langmuir probe measurements on LM thruster) [41]
<i>Double Ion Current Fraction</i>	ExB probe measurements in LDT and on LM thruster [15, 33]	ExB probe measurements of centerline values [15, 33]	ExB probe measurements on EM thruster [42]	ExB probe measurements on EM thruster [42]	ExB probe measurements on PMIR thruster [42]
Downstream Plasma Properties					
<i>Plasma Potential</i>	Emissive probe measurements of 3-5 V from NSTAR LDT and an average measured value for V _g of about 10V [33, 37]	Emissive probe measurements of 3-5 V from NSTAR LDT and an average measured value for V _g of about 10V [33, 37]	Emissive probe measurements of 3V from LM thruster [43] and an average measured value for V _g of about 10V from 2000 hour test	Emissive probe measurements of 3V from LM thruster [43] and an average measured value for V _g of about 10V from NEXT LDT	Emissive probe measurements of 3V from LM thruster [43] and an average measured value for V _g of about 10V from NEXT LDT
<i>Electron Temperature</i>	Measurements from DS1 [44]	Measurements from DS1 [44]	2 eV; assumed to be similar to NSTAR	2 eV; assumed to be similar to NSTAR	2 eV; assumed to be similar to NSTAR
Neutral Gas Properties					
<i>Upstream Neutral Density</i>	Average value, calculated from measured beam current, propellant efficiency, accelerator grid open area fraction, and chamber temperature [47]	Average value, calculated from measured beam current, propellant efficiency, accelerator grid open area fraction, and chamber temperature [47]	Average value, calculated from measured beam current, propellant efficiency, accelerator grid open area fraction, and chamber temperature [48]	Average value, calculated from measured beam current, propellant efficiency, accelerator grid open area fraction, and chamber temperature [48]	Average value, calculated from measured beam current, propellant efficiency, accelerator grid open area fraction, and chamber temperature [48]
<i>Vacuum Chamber Pressure</i>	Measured value, gauge calibrated on Xe [33]	Measured value, gauge calibrated on Xe [38]	Measured value, gauge calibrated on N ₂ , corrected for Xe [39]	Measured value, gauge calibrated on N ₂ , corrected for Xe using scale factor of 2.5	N/A

Table A1 Sources of data used to define CEX2D and CEX3D code input parameters (continued)

Parameter	NSTAR 8200 Hour LDT	NSTAR 30,352 Hour ELT	NEXT 2000 Hour Test	NEXT 51,184 Hour LDT	NEXT Space Conditions
<i>Neutral Gas Properties (continued)</i>					
<i>Upstream Gas Tem- perature</i>	Based on dis- charge chamber temperatures measured in EM thruster [47]	Based on dis- charge chamber temperatures measured in EM thruster [47]	Based on dis- charge chamber temperatures measured in PM1 thruster [48]	Based on dis- charge chamber temperatures measured in PM1 thruster [48]	Based on dis- charge chamber temperatures measured in PM1 thruster [48]
<i>Accelerator Grid Tem- perature</i>	Based on accel- erator grid stiffener temperatures measured in NSTAR EM thruster [47]	Based on accel- erator grid stiffener tem- peratures measured in NSTAR EM thruster [47]	Based on accel- erator grid stiffener tem- peratures measured in PM1 thruster [48]	Based on dis- charge chamber temperatures measured in PM1 thruster [48]	Based on dis- charge chamber temperatures measured in PM1 thruster [48]
<i>Downstream Gas Tem- perature</i>	Chamber wall temperature	Chamber wall temperature	Chamber wall temperature	Chamber wall temperature	N/A